ATLAS PUB Note
ATL-DAQ-PUB-2024-002
19th November 2024

Trigger Studies with Event Filter Tracking at the HL-LHC

The ATLAS Collaboration

The Event Filter Tracking system will allow for real-time charged-particle trajectory reconstruction for the trigger of the ATLAS experiment in the High-Luminosity LHC era. While the system is still under design, this note presents an overview of the effects of trading off tracking performance in the trigger for increased event processing throughput. The performance of trigger selections for different physics objects are studied, with particular emphasis on those that depend heavily on tracking. Different tracking scenarios are emulated by degrading the performance of the offline track reconstruction as measured on simulated data from the new all-silicon inner tracker, for example by reducing the tracking efficiency and worsening the resolution of some critical track parameters. Depending on the performance required on the trigger in Run 4, each possible tracking scenario can help guide and tune the design of the Event Filter Tracking system by quantifying the signal efficiency and background rejections.

1 Introduction

This note presents performance studies related to the Event Filter (EF) Tracking project of the ATLAS experiment [1], a part of its Phase-II upgrade program for the High-Luminosity LHC (HL-LHC) phase. EF Tracking will implement a possibly heterogeneous computing system for real-time tracking algorithms, which is described in detail in the Phase-II TDAQ TDR Amendment [2]. The goal of this note is to link the quality of tracks, reconstructed online by EF Tracking, to the overall performance of the trigger selections that will be deployed in ATLAS for HL-LHC; for each trigger selection, results are shown for the key physics objects that particularly benefit from EF Tracking. The HL-LHC pile-up conditions will produce an average of 200 inelastic proton-proton collisions per bunch crossing, and a new full-silicon Inner Tracker (ITk) [3, 4], designed to allow efficient tracking in such environment, will be installed during the Phase-II upgrade. The rate at which events may be reconstructed for a given quantity of computational hardware is however a much more critical driving factor in the design for the EF than it is for offline, with tracking historically being the most computationally expensive reconstruction performed at the EF stage. It is therefore important to study how the ATLAS physics goals are affected by degraded tracking performance parameterisations, the likes of which may be achieved by the tracking solutions with the highest throughput.

Since the EF Tracking is still under design, the offline track reconstruction in Run 4 is taken as a baseline reference, defining an upper limit on the online performance. The EF Tracking is emulated by degrading offline tracks in terms of reconstruction efficiency and resolution on the transverse momentum (p_{T}) and on the impact parameters (d_0 and z_0), defined in the ATLAS coordinate system [1] and by applying minimum p_{T} cuts corresponding to different operational scenarios. Finally, an enhancement of track duplicates is considered as an additional tracking quality degradation scenario for some specific trigger selections. Depending on the trigger signature, the algorithms reconstructing the physics objects of interest are emulated starting from those operating online during Run 3 [5] or currently foreseen for offline reconstruction in the Phase-II upgrade context.

With the above methodology, multiple trigger signatures are studied, to investigate use-cases amongst different physics benchmarks. For each of these signatures, various EF Tracking scenarios are emulated and compared to the nominal case, corresponding to the usage of offline-quality track reconstruction.

This document is organized as follows. After a brief overview of the EF Tracking project in Section 2, the adopted methodology is detailed in Section 4, while the studies performed on different trigger selections and their results are reported in Section 5.

2 Overview of the EF Tracking project

The detector data volume that will be produced by the high pile-up conditions foreseen at the HL-LHC represents a significant challenge to the ATLAS Phase-II TDAQ system, whose architecture and physics motivations are described in the Phase-II TDAQ TDR [6]. Further updates, including the EF Tracking

[1] ATLAS uses a right-handed coordinate system with its origin at the nominal interaction point (IP) in the centre of the detector and the z-axis along the beam pipe. The x-axis points from the IP to the centre of the LHC ring, and the y-axis points upwards. Polar coordinates (r, ϕ) are used in the transverse plane, ϕ being the azimuthal angle around the z-axis. The pseudorapidity is defined in terms of the polar angle θ as $\eta = -\ln\tan(\theta/2)$ and is equal to the rapidity $y = \frac{1}{2}\ln\left(\frac{E+p_z c}{E-p_z c}\right)$ in the relativistic limit. Angular distance is measured in units of $\Delta R \equiv \sqrt{(\Delta y)^2 + (\Delta\phi)^2}$.

strategy, are presented in the Phase-II TDAQ TDR Amendment [2]. All the EF algorithms, including the EF Tracking ones, will run on a flexible, heterogeneous commercial system consisting of CPU cores possibly helped by commodity accelerators, such as GPUs and FPGAs, if needed to bear the requested computing load.

The TDAQ design foresees that events are processed by a first hardware trigger (Level-0), basing its decision on calorimeter and muon detector data, and those which are accepted are passed to the EF, which gathers the data from all the detector readout systems at a maximum rate of 1 MHz. After the EF processing, the rate of accepted events is reduced to 10 kHz. The HL-LHC trigger algorithms will face numerous challenges, already at Level-0. The calorimeter energy resolution and isolation effectiveness are reduced due to pile-up, while multi-object selections will cope with more random coincidences of objects coming from different independent collisions, all leading to the choice to allow for a large Level-0 output trigger rate.

Track reconstruction performed on data from the ITk system will then play a crucial role in the subsequent trigger selections, to achieve a manageable EF output rate. Tracking can be used to refine the selection of trigger objects identified at Level-0, to improve the estimate of their kinematic properties and to reduce the rate of multi-object coincidences, for example by requiring their associated tracks to come from the same collision vertex. The tracking task itself however becomes more challenging because of the large rate at which it has to operate and of the high density of hits in tracking detectors, which makes pattern recognition more computationally intensive. At the same time, the optimised layout of the ITk tracker is expected to allow a reduction of the fake tracks rate to a negligible level [3, 4].

To investigate the trigger scenarios for Run 4, the trigger menu studied for the ATLAS data-taking during the HL-LHC in Ref. [2] has been taken as reference, and is reported in Table 1. While this is the latest complete collection of selections for Run 4, there are multiple ongoing studies to optimise these selections with new techniques, that will possibly extend these baselines. The studies presented in this document are based on the assumptions of this representative menu, with the caveat that it may evolve before the start of Run 4, possibly requiring an update of the EF Tracking strategy.

The table shows for each primary trigger selection the expected thresholds for HL-LHC, together with the corresponding offline thresholds at full efficiency for the past runs. Thanks to the Phase-II upgrades, ATLAS trigger operation is expected to allow lower trigger thresholds than those used in Run 2 for most of the triggers, despite the challenging data-taking conditions. In the table the expected rates are also shown after each trigger level: first at Level-0, then with "regional tracking" that is run only in Regions of Interest (RoI) defined based on objects identified at Level-0, and lastly after the full EF selection. The regional tracking provides a factor three rate reduction in the total rate, becoming a factor five for single leptons and as high as a factor twelve for missing transverse energy ($E_{\mathrm{T}}^{\mathrm{miss}}$) triggers.

To increase flexibility, two processing options are foreseen for the tracking task:

- **regional tracking running at 1 MHz**: reconstruction of tracks with $p_T > 2$ GeV only in RoIs, accounting for roughly 5% of the detector acceptance;
- **full-scan tracking running at 150 kHz**: reconstruction of tracks with $p_T > 1$ GeV in the whole ITk detector acceptance, i.e. up to $|\eta| < 4$.

The balance between the two different tracking processing options will be optimised to maximise acceptance for different objects, and will be subject to change, according to the trigger menu, available resources, and output rate requirements. Consequently, in this note both options are investigated for the trigger selections under study, in order to document their corresponding impact and regardless of their final baseline definition.

Table 1: Representative trigger menu for 1 MHz Level-0 rate, studied in Ref. [2] and reported here. The offline p_{T} thresholds indicate the momentum above which a typical analysis would use the data. Cases where numbers span more columns, the same Level-0 trigger seeds multiple EF triggers. For multi-object triggers, the corresponding threshold of each object is listed and separated by commas.

	Offline p_{T} Threshold [GeV]		Planned HL-LHC		After	Event
	Run 1	Run 2	Offline p_{T}	Level-0 Rate	regional tracking	Filter Rate
Trigger Selection		(2017)	Threshold [GeV]	[kHz]	[kHz]	[kHz]
isolated single e	25	27	22	200	40	1.5
isolated single μ	25	27	20	45	45	1.5
single γ	120	145	120	5	5	0.3
forward e			35	40	8	0.2
di-γ	25	25	25,25		20	0.2
di-e	15	18	10,10	60	10	0.2
di-μ	15	15	10,10	10	2	0.2
$e-\mu$	17,6	8,25 / 18,15	10,10	45	10	0.2
single τ	100	170	150	3	3	0.35
di-τ	40,30	40,30	40,30	200	40	0.5†††
single b-jet	200	235	180	25	25	0.35†††
single jet	370	460	400			0.25
large-R jet	470	500	300	40	40	0.5
four-jet (w/ b-tags)		45†(1-tag)	65(2-tags)	100	20	0.1
four-jet	85	125	100			0.2
H_{T}	700	700	375	50	10	0.2†††
$E_{\mathrm{T}}^{\mathrm{miss}}$	150	200	210	60	5	0.4
VBF inclusive			2x75* ($\Delta\eta > 2.5$ & $\Delta\phi < 2.5$)	33	5	0.5†††
B-physics††				50	10	0.5
Support Triggers				100	40	2
Total rate				1066	338	10.15

† In Run 2, the 4-jet b-tag trigger operates below the efficiency plateau of the Level-1 trigger.

†† This is a place-holder for selections to be defined.

††† Assumes additional analysis-specific requirements at the Event Filter level.

* Refers to two 75 GeV jets.

In the document, they are distinguished by the minimum p_{T} of the reconstructed tracks: 1 GeV for the full-scan and 2 GeV for the regional scenario.

The representative trigger menu shown in Table 1 demonstrates the critical role of EF Tracking in achieving the expected rate reduction, as reported in the last columns of the table, obtained by combining tracking information with refined calorimeter and muon reconstruction in the EF. The corresponding required signal selection and background rejection capabilities can thus be used in this document as a benchmark for the performance of EF Tracking applications.

3 Monte Carlo samples

Several simulated Monte Carlo samples have been used in these studies, reproducing proton-proton (pp) collisions at the center-of-mass energy of 14 TeV in the HL-LHC pile-up scenario, with an average number of visible proton-proton interactions per bunch crossing $\langle\mu\rangle$= 200. All these samples are generated with Powheg [7] interfaced with Pythia 8 [8] for parton shower and hadronization. The samples used specifically for each study are detailed in the corresponding sections. To extract the tracking performance, samples of single particles are generated with Geant4 [9] `ParticleGun`, following the detector coverage and beam-spot size, and mixed with the expected pile-up. Trigger rates and background rejections are studied with a sample of di-jet events at $\langle\mu\rangle$= 200, generated using Pythia 8 and applying multiple filters on jet p_{T} to increase the generation efficiency.

All samples are processed with the Geant4 ATLAS full detector simulation [9, 10], including the latest ITk layout [2] described in Ref. [11]. The offline tracks are reconstructed following the criteria described in Ref. [12] and physics particles are consequently reconstructed and identified using the standard ATLAS software suite [13].

4 Emulation of the EF Tracking performance

Since the EF Tracking system is still under design and the trigger algorithms expected for HL-LHC are still under development, there is no reliable full simulation of the upgraded ATLAS trigger. To provide information for the studies presented in this document, the full simulation is substituted with an emulation-based approach, derived with the following assumptions:

- Level-0 trigger decisions are emulated with offline-reconstructed objects, such as muons and jets, to provide a reasonable input to the EF algorithms; trigger thresholds are adapted, to take into account the different resolutions for online and offline;
- the EF Tracking performance is emulated using offline tracks as proxies and applying a set of possible degradation scenarios, as described in details in section 4.1;
- for each specific trigger selection, offline algorithms are adopted, as already happening in many Run 3 triggers; results are obtained testing these algorithms on the emulated EF Tracking tracks.

[2] The bulk of the samples are simulated with `ATLAS-P2-RUN4-01-00-00`, few samples include new geometry tags(for example `ATLAS-P2-RUN4-03-00-00`). The difference between these geometries is considered negligible for these studies (only concerning the placement of some ITk endcap rings and a minor update of the HGTD geometry).

4.1 Tracking performance emulation

A tracking emulation tool has been developed to be commonly used across multiple ATLAS upgrade studies [14]. This is designed to operate on offline-reconstructed tracks, or even simulated truth-particles, degrading their quality to provide a proxy for online tracking studies. Different EF Tracking degradation scenarios are studied and presented with corresponding scaling factors (SF) either on the tracking efficiency or on the track parameter resolution. All the scenarios are compared to the nominal case, corresponding to a scenario obtained using offline-quality tracks. For all the results presented here, the tracking emulation was used to:

- apply a flat reduction of the tracking efficiency, randomly removing a specified fraction of tracks (represented by efficiency SF), regardless of their kinematics and of their origin, so that no distinction is made between signal and fake tracks;
- smear the track p_{T}, d_0 and z_0 (represented by resolution SF), that are modified with a Gaussian spread modelled on the offline resolution (measured with respect to truth); the reconstructed uncertainties on the smeared quantities are adjusted accordingly;
- apply a cut on the minimum reconstructed transverse momentum, allowing to emulate the different choices for full-scan and regional tracking (p_{T} >1 GeV and p_{T} >2 GeV respectively); for reference, offline tracks are reconstructed with a minimum p_{T} of 900 MeV in $|\eta|$ <2 and of 400 MeV in the forward regions;
- implement a simplified track duplication mechanism, that reproduces fake track distributions unavailable in the current simulation; the impact of fake tracks is expected to be negligible for most signatures, but can affect critically some specific use-cases, e.g. when evaluating isolation criteria; in the track duplication emulation, any original offline track is duplicated following a fixed duplication probability and then modified following the above smearing rules, with no other changes in the coordinates; this simple approach has a realistic effect only for selections based on track counting and is adopted only for muon isolation and tau identification.

No explicit correlation is enforced between different tracks and different degradation effects. Nevertheless, to reproduce the fact that the tracking performance of real systems varies with the region of the detector considered, different track degradation scenarios are applied in different kinematic regions.

The next two subsections describe the extraction of the offline track parameters resolution as a function of p_{T} and η and the way reconstructed parameters can be modified in order to emulate the desired performance scenario.

4.1.1 Modelling the resolution of track parameters

The resolution on track parameters for offline reconstruction is derived from Monte Carlo simulations of ATLAS in Run 4. In particular, three single-muon samples are taken as reference, each representing muons at fixed p_{T} values: 1, 10, and 100 GeV. The procedure to extract and model the resolution on a given track parameter as a function of p_{T} and η proceeds as follows:

- a binning in η is defined, to account for differences in the various detector regions;

- for each η bin in each single-muon sample, the residuals of reconstructed parameters with respect to their truth value are modeled with a Gaussian distribution, whose width is interpreted as the resolution on the parameter;
- for each η bin, the p_{T} dependency is parameterized through fitting the resolutions obtained in the three samples with a power series; Figure 1(a) shows an example for the z_0 parameter;
- a two-dimensional histogram in (η, p_{T}) is built using the above parameterization; Figure 1(b) shows the resolution map obtained for z_0;
- the above histogram is re-binned to have six p_{T} bins (with edges at 1., 1.5, 2.5, 5., 10., 20., 100. GeV); for each p_{T} bin, the η-dependency is parameterized through a fit with a sum of a polynomial and a Gaussian function; Figure 1(c) shows an example of parameterized z_0 resolution as a function of pseudo-rapidity for a single p_{T} bin.

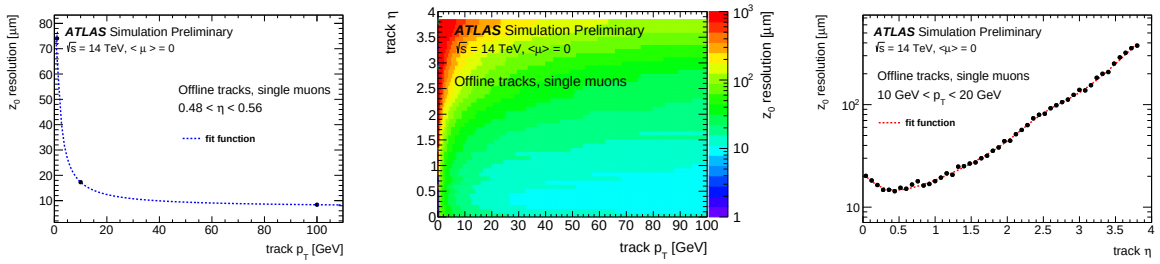

(a) (b) (c)

Figure 1: (a) Example of z_0 resolution behaviour as a function of p_{T} in one η-bin and corresponding best fit; (b) two-dimensional z_0 resolution parametrised as a function of p_{T} and η; (c) example of z_0 resolution behaviour as a function of η in one p_{T} bin and corresponding best fit.

4.1.2 Emulating track parameter degradation scenarios

The track parameter resolution is modified by applying a Gaussian smearing on the chosen track parameters, with a width expressed in units of their original resolution (in bins of η and p_{T}) multiplied by a given scaling factor (SF). Unless stated otherwise, the smearing procedure is applied simultaneously to p_{T}, d_0 and z_0. For this purpose the parameterizations of the resolution functions of the offline tracks in bins of η and p_{T}, obtained as described in Section 4.1.1, are used. This means that, when a given resolution SF = X is applied to offline tracks, the final resolution is $\sqrt{1 + \mathrm{X}^2}$ times the original one. If SF = 0, no resolution smearing is applied, while the rest of the degradation remains (e.g. the minimum p_{T} cuts). With the same technique, the smearing is applied to the covariance matrix of the track parameters, neglecting correlations. An example is shown in Figure 2(a) and 2(b) for d_0 and its uncertainty, for tracks associated to jets before the b-jet selection.

5 Performance of trigger selections with different tracking scenarios

This section describes the studies carried out on a variety of trigger selections that benefit from the use of the online tracks and shows the impact on their performance due to possible reductions in track quality. All

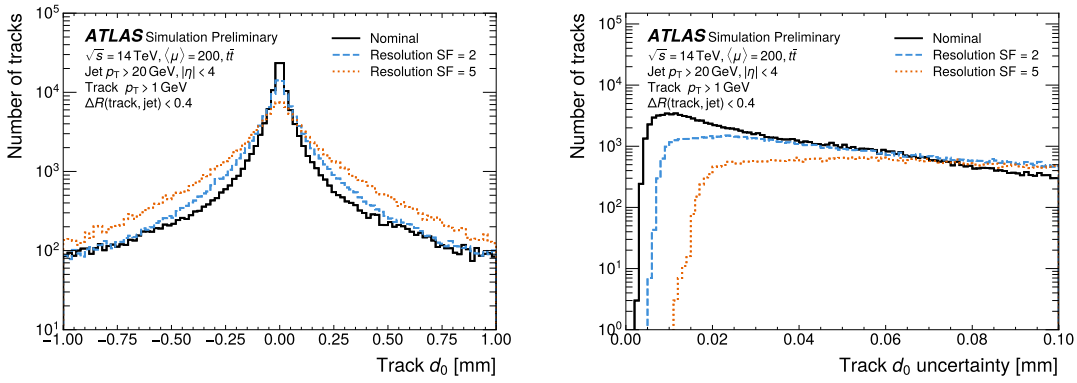

(a) (b)

Figure 2: Distributions of (a) the d_0 track parameter and (b) its uncertainty, for tracks associated to jets used to become b-jet candidates. The impact of different resolution scale factors is compared to the nominal performance ($SF = 0$).

the studies follow the same emulation strategy described above, and if not stated otherwise, all their results are calculated with respect to the emulated Level-0 selection.

The main strategy to assess the performance for the EF selections is to evaluate the efficiency on target physics signals, along with the corresponding rejection on the most abundant background components, when possible. The signal efficiency for each algorithm is measured on events defined as signal at Monte Carlo level or passing the corresponding offline selection. The rejection factor corresponds to the number of background events processed by the trigger selection divided by the number of those it actually selects. Where relevant, results are presented for both the regional and full-scan tracking scenarios, requiring respectively a minimum track p_{T} of 2 GeV and 1 GeV.

5.1 Muon trigger selections

The representative trigger menu summarized in Table 1 includes a 20 GeV single isolated muon trigger and a 10 GeV di-muon trigger. As a reference for this study, the primary Run 3 working point is designed to grant a minimum trigger efficiency of 98%, for muons with momenta above 10 GeV.

These studies focus on both muon reconstruction and isolation algorithms. Two main signal samples are considered:

- single muons with p_{T} above 1 GeV, uniformly distributed in $1/p_{\mathrm{T}}$ and η;
- muon pairs from $Z \rightarrow \mu^+\mu^-$ decays.

Isolation studies are based on samples of $t\bar{t}$ pairs decaying to hadrons, where semi-leptonic decays of B hadrons provide a source of non-isolated muons.

In Run 4, the Level-0 muon selection will be provided by the high precision MDT trigger. To emulate this trigger selection, offline standalone muons are considered, which consist of tracks reconstructed in the muon spectrometer and extrapolated to the region of the inner silicon tracker, without any ITk track matching

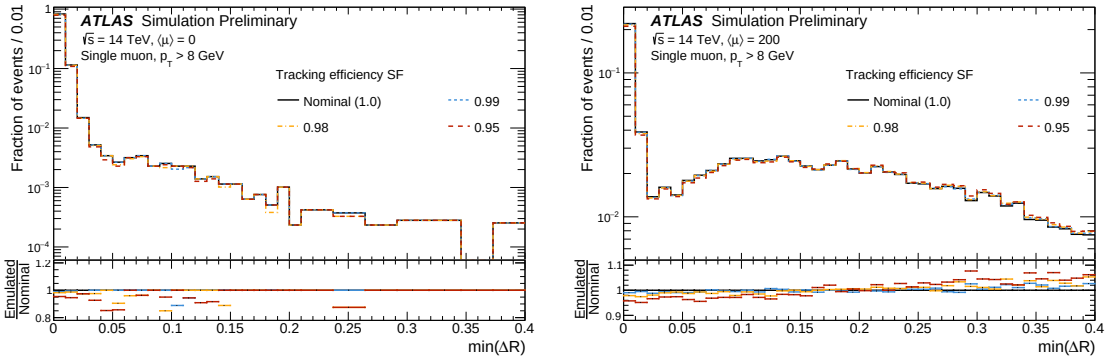

(a) (b)

Figure 3: Distributions of the minimum ΔR between standalone muon candidates and EF Tracking emulated tracks used to find the matching, in single muon events (a) with $\langle\mu\rangle = 0$ and (b) with $\langle\mu\rangle = 200$; different degradation scenarios are compared in both plots together with the true distributions.

requirement. These muons' p_{T} are required to exceed 8 GeV or 10 GeV to emulate the Level-0 thresholds, which then seed the EF muon selections with p_{T} thresholds of 10 GeV and 20 GeV, respectively.

The EF trigger selection is based on combined muons, which require a combination of standalone muons and EF Tracking tracks, to improve the track parameter resolution and reduce fake components. In a subsequent step, additional EF Tracking tracks found in a cone around the matched track are used to compute variables connected to the muon isolation. These two steps are separately considered in the following sections.

5.1.1 Muon-track matching efficiency studies

Standalone muons used as a proxy for those passing the Level-0 trigger are matched to EF Tracking tracks within a $\Delta R < 0.1$ cone, to form combined muon candidates. Their transverse momentum is evaluated averaging the p_{T} measurements of the standalone muon and of the leading-momentum matched track. This approach is a simplified emulation of the muon trigger algorithm adopted in Run 3, which also makes use of the perigee parameters of the standalone muon extrapolated to the beam axis, which are not available for this study.

Figure 3(a) and 3(b) show the minimum ΔR between standalone muon candidates and the candidate ITk tracks used for the matching, measured in single muon samples without and with pile-up respectively, for different EF Tracking degradation scenarios. The shape of these distributions motivates the choice of a cone size of $\Delta R < 0.1$, which ensures a high probability to have at least one track within the cone with no pile-up included.

The efficiency to combine standalone muons to ITk tracks is then evaluated with respect to truth, for the two trigger thresholds under study. For this calculation, standalone muons passing a slightly lower Level-0 threshold (8 GeV for the low-p_{T} and 10 GeV for the high-p_{T}), are required to match a truth signal muon. Results are reported as a function of the true muon p_{T} and η for single muon samples with and without nominal HL-LHC pile-up in Figures 4. For comparison, also the turn-on expected for the emulated Level-0 muons (standalone) at the same threshold are shown to underline the improvement in the turn-on slope due

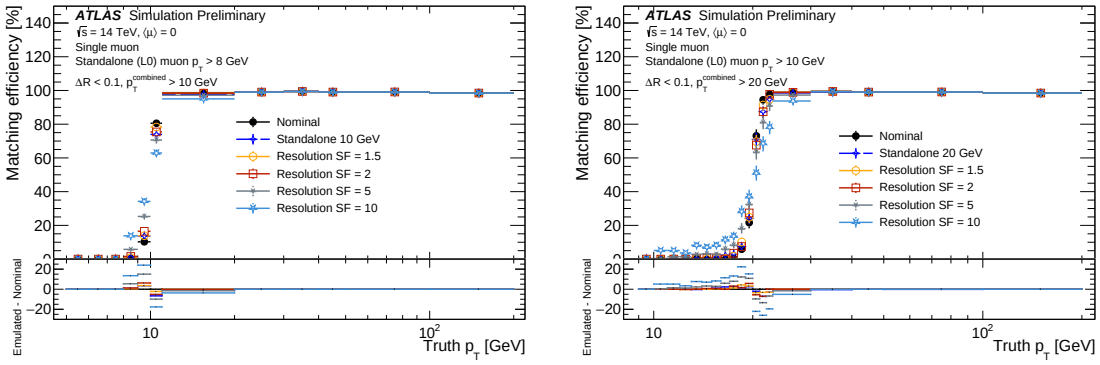

(a)

(b)

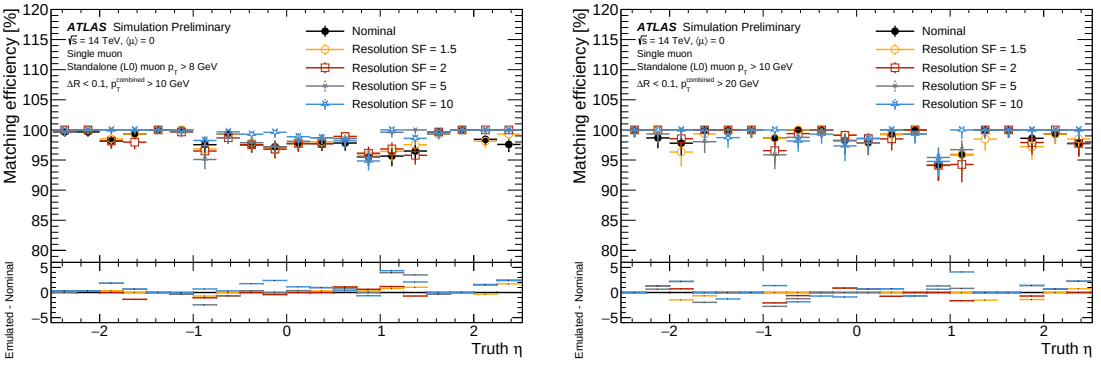

(c)

(d)

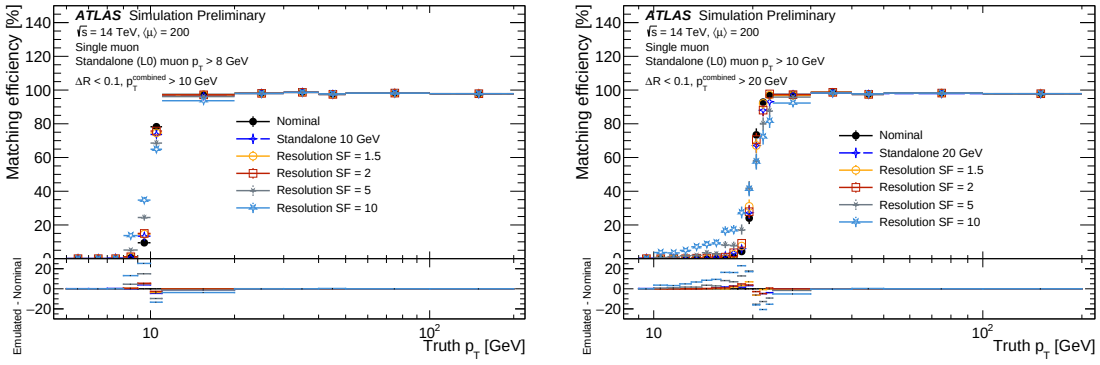

(e)

(f)

Figure 4: Efficiency of combined muons with respect to truth as a function of the truth muon p_{T} and η for single muon events, emulating low-p_{T} (p_{T} >10 GeV) and high-p_{T} (p_{T} > 20GeV) trigger selections, with different tracking resolution degradation scenarios: (a) (c) low-p_{T}, no pile-up, (b) (d) high-p_{T}, no pile-up, (e) low-p_{T} with $\langle\mu\rangle = 200$, (f) high-p_{T} with $\langle\mu\rangle = 200$. Combined muons result from the matching of a standalone muon and the closest track in a cone $\Delta R < 0.1$. Standalone muons have $p_{\mathrm{T}} > 8$ GeV in the low-p_{T} case and p_{T} >10GeV in the high-p_{T} one, emulating the expected Level-0 selections. For comparison, the turn-on expected for these emulated Level-0 muons are shown.

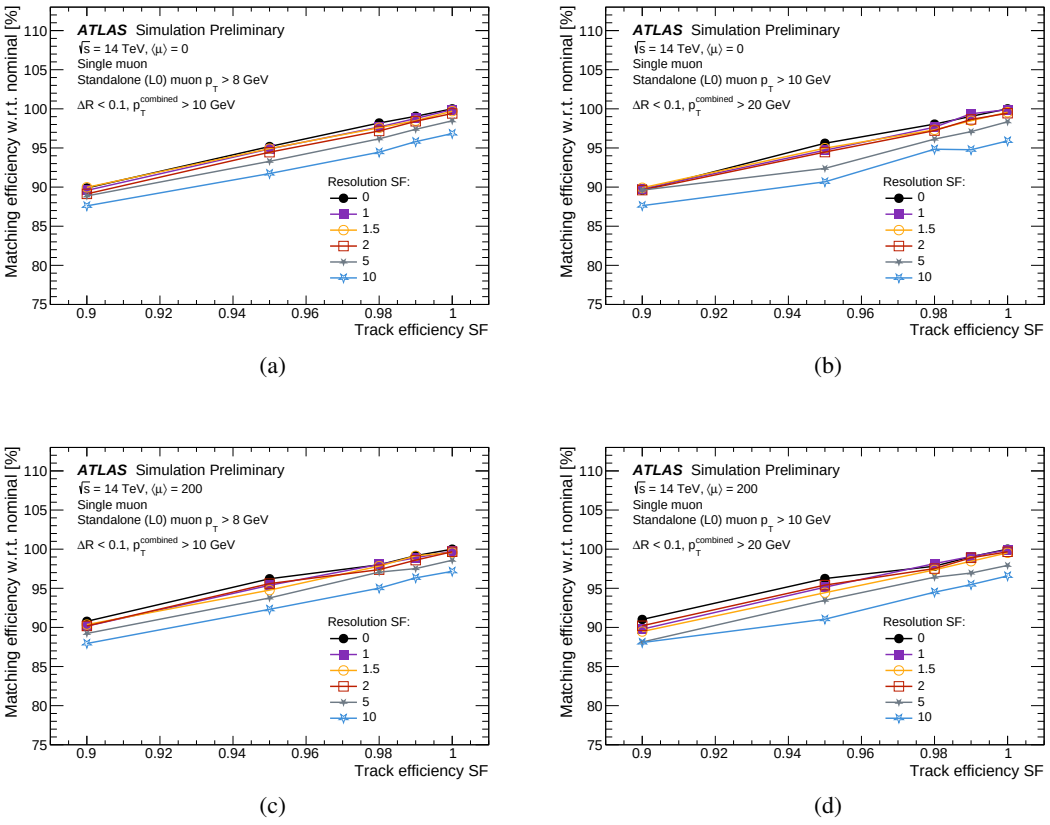

Figure 5: Efficiency of the emulated combined muons with respect to the nominal case (with efficiency SF=1, and no resolution smearing), where offline tracks are used, for different tracking efficiency and resolution degradation scenarios; the measurement is performed with single muon events with (a) no pile-up, 10 GeV p_{T} threshold, (b) no pile-up, 20 GeV p_{T} threshold, (c) with $\langle\mu\rangle = 200$, 10 GeV p_{T} threshold, (d) with $\langle\mu\rangle = 200$, 20 GeV p_{T} threshold. Standalone muons, emulating the Level-0 selections, have $p_{\mathrm{T}} > 8$ GeV and 10 GeV in the low-p_{T} and high-p_{T} cases respectively. Combined muons are the results of the matching of a standalone muon and the closest track in a cone $\Delta R < 0.1$.

to the track-matching. The effects of the degradation of the p_{T} resolution is clearly visible in the turn-on region. The plots also show a non-negligible low-momentum tail in the scenario when the p_{T} resolution is at its worst values. These are combined muons matched with tracks with badly reconstructed p_{T}, which is much larger than the truth value, so tend to pass the trigger threshold.

The integrated efficiency of the muon-track combination is calculated for different tracking performance scenarios, for true muons above the EF p_{T} threshold. Results are reported in Figure 5 as the ratio with respect to the efficiency obtained in the nominal case, where no tracking degradation is emulated. As expected, the relative efficiency is proportional to the applied tracking efficiency scale factor, while the effect of the p_{T} smearing is only marginal, with reduced efficiency with larger smearing because of the slower turn-on. The same trend is visible with and without pile-up, and for both low-p_{T} and high-p_{T} selections.

5.1.2 Muon isolation studies

An additional isolation requirement can be applied to EF muon candidates, after being confirmed by the track-matching procedure. Isolation criteria are based on the track counting in a cone around the matched track and are studied for the EF Tracking full-scan configuration. Results are presented for the following preliminary isolation definition:

- a $\Delta R < 0.3$ cone is opened around the EF Tracking track that matches the standalone muon candidate;
- the EF Tracking tracks within the cone are required to have $p_{\mathrm{T}} > 1$ GeV;
- these are further required to satisfy the condition $|(z_0 - z_{PV}) \cdot \sin(\theta)| < z_{\mathrm{cut}}$, where z_0 and θ are the track parameters, z_{PV} is the z position of the primary vertex with the highest $\sum p_T^2$ for associated tracks and z_{cut} is a cut, defined as a function of track p_{T} and η, ranging from 0.6 to 6 mm;
- the muon candidate passes the isolation criteria if the sum of the p_{T} of the selected tracks is below 20% of the muon candidate p_{T}.

The requirement on $z_0 \cdot \sin(\theta)$ is meant to reject pile-up tracks [15] and the applied cut is tighter for low p_{T} tracks, in order to give less weight to pile-up contamination, and looser at high p_{T} in order to better include genuine jet tracks; the cut is also designed to take into account the dependence of z_0 resolution and of jet track purity on η and p_{T}.

Muon isolation is studied only in the full-scan tracking scenario, but results are expected to be valid also for the regional tracking case, since both the isolation calculation, based on p_{T} sums, and the sliding z_0 window selection, give larger weight to higher p_{T} tracks.

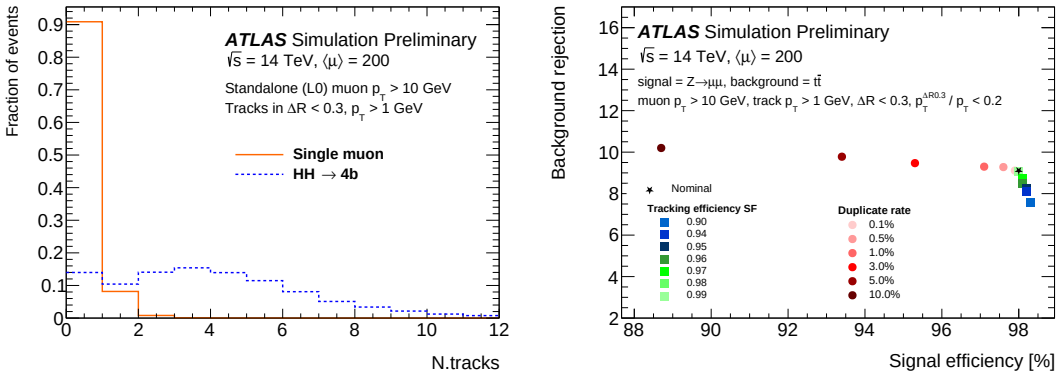

(a) (b)

Figure 6: (a) Number of tracks contributing to the muon track isolation requirement (within a cone of $\Delta R < 0.3$) and muon $p_{\mathrm{T}} > 10$ GeV, for single muon samples (signal) and $HH \rightarrow 4b$ events (background), both with $\langle\mu\rangle = 200$; no smearing factor is applied in the EF Tracking emulation. (b) Performance of the isolation selection in terms of signal efficiency, evaluated on $Z \rightarrow \mu\mu$ decays, and background rejection, evaluated on fully hadronic $t\bar{t}$ events, for different combinations of the EF Tracking efficiency and track duplication probability; both signal and background samples include pile-up at $\langle\mu\rangle$= 200; efficiencies and rejections are evaluated on muon candidates with p_{T} above 10 GeV, passing the track matching criteria and corresponding to a true simulated muon. Isolation requires that the sum of the momenta of the tracks with $p_{\mathrm{T}} >1$ GeV included within a $\Delta R < 0.3$ cone around the candidate muon is less than 20% of the muon p_{T}.

Figure 6(a) shows an example of the distribution for the number of EF Tracking tracks contributing to the isolation requirement, comparing the case of isolated muons from Z boson decays with muons in jets stemming from semi-leptonic B-hadron decays.

To study muon isolation performance, the track duplication mechanism is adopted. Figure 6(b) summarizes the performance of the isolation selection in terms of signal efficiency, evaluated on $Z \to \mu\mu$ decays, and background rejection, evaluated on fully hadronic $t\bar{t}$ events, in different scenarios for EF Tracking efficiency and track duplication probability. Results are reported for muon candidates passing the track matching criteria and corresponding to a true simulated muon. The reduction of tracking efficiency has a limited impact on signal efficiency, while it negatively affects the background rejection, as some jet tracks will not pass the selection used to define isolation variables. Track duplication instead tends to make both signal and background appear as less isolated, with a consequent reduction of signal efficiency and increase of background rejection; the effect becomes significant above a duplication probability of $\sim 1\%$. Finally, isolation criteria are found to be only marginally affected by track kinematics and parameter estimation quality, thus results for resolution degradation are not reported.

5.2 Electron trigger selections

The representative trigger menu summarized in Table 1 includes a 22 GeV isolated single electron trigger and a 10 GeV di-electron trigger. As a reference for this study, typical Run 3 working points for this trigger selection are designed to achieve a minimum trigger efficiency of 98% for electrons with transverse momentum above 10 GeV; lower efficiencies of 97% are expected for softer electrons, due to bremsstrahlung effects.

This study focuses on the impact of track quality on the efficiency of electron identification. The signal sample considered for this purpose contains electron pairs from $Z \to e^+e^-$ decays, which provides enough statistics in the relevant electron momentum range, around 10-20 GeV. The typical background to this selection is represented by di-jet events, where jets can be misidentified as electrons.

Electron reconstruction is studied up to $|\eta| < 2.5$, with exactly the same algorithms used in Run 3, making them use the current ATLAS calorimeter and the ITk tracking system in the new pile-up environment of HL-LHC. The extension to the forward region, which is expected by the increased pseudo-rapidity coverage of ITk up to $\eta = 4$, is still under study and not included in this note.

The Level-0 selection makes use of fine-granularity cell information from the LAr calorimeter. At the EF the reconstruction of electron candidates proceeds through a match between calorimeter clusters above threshold and EF Tracking tracks. In this process, tracks are refitted with a Gaussian-sum filter (GSF) algorithm [16], to take into account the non Gaussian distribution of the stochastic terms involved in the track fitting due to electron radiative effects. In a subsequent step, data from both the tracking and the calorimeter detector systems is combined to build the variables used for a likelihood-based (LH) electron identification, allowing to reject fake candidates. To further increase the rejection power against fake candidates, track-isolation is considered, to distinguish prompt lepton production from hadronic decays. To quantify the amount of activity in the proximity of the candidate electron, the sum of the transverse momenta of the tracks in a cone around the candidate is used. These two steps are individually described in the following sections. The studies presented in this note are focusing only on the effects of the tracking deterioration on the electron identification efficiency on signal, while the rejection of background is postponed to later studies, given the absence of a good emulation of the calorimeter background at Level-0.

For this reason the efficiencies are measured with respect to offline, without taking into account any Level-0 preselection.

5.2.1 Electron identification efficiency studies

To correctly address the electron trigger performance, the EF Tracking emulation is applied to offline GSF-refitted tracks, and electron candidates are then formed using the smeared tracks in combination with clusters of energy in the calorimeter. Tracks with p_{T} greater than 1 GeV are considered. The efficiency of the EF electron identification is measured with respect to offline candidates associated to true simulated electrons with $p_{\mathrm{T}} > 10$ GeV. In particular, a geometrical match between the trigger and offline objects is required within $\Delta R < 0.15$, selecting the highest-p_{T} electron in the cone. The offline reference candidates are also required to pass the tight offline identification selection [17]. Figure 7 shows the tight electron identification efficiency versus p_{T} and η for different tracking efficiency degradation scenarios, measured on $Z \rightarrow ee$ events with and without the additional pile-up collisions. These results show that the applied tracking efficiency SF is directly reflected in the overall electron reconstruction efficiency. Figures 7(e) and 7(f) show the same efficiency as a function of η in two different p_{T} regimes, between 10 and 20 GeV and above 20 GeV with pile-up compared to possible working points in the two p_{T} regimes. This shows that maintaining the tracking efficiency above 98% preserve these targets.

In addition, the track parameter resolution proves to be a key ingredient in the electron identification process, as demonstrated by the effects shown in Figure 8 for different tracking resolution degradation scenarios. As above, Figure 8(e) and 8(f) show the efficiency as a function of η, separated for two different momentum regimes, low p_{T} and high p_{T} with pile-up and the comparison with the expected working points allows for a safe maximum tracking degradation of factor 2 worst than offline.

5.2.2 Electron isolation studies

Track isolation is of critical importance for distinguishing electrons and jets, thus reducing the most abundant background for this selection. Isolation mechanism is described in [17] and the applied criteria are defined by:

- opening a cone around the electron candidate; the cone size is defined as a function of the electron candidate momentum and becomes smaller at higher p_{T};
- selecting tracks within the cone that fulfill the requirement $|(z_0 - z_{PV}) \cdot \sin(\theta)| < 3$ mm, where z_0 and θ are the track parameters and z_{PV} is the z position of the primary vertex with the highest $\sum p_T^2$ for associated tracks; this step is meant to select tracks that originate from the primary vertex and to reduce the pile-up contribution;
- summing the p_{T} of the selected tracks and evaluating the ratio between this sum and the momentum of the electron candidate.

In this study on each electron passing the tight identification requirement described above, a loose track isolation requirement is applied, which corresponds to a maximum cone size of $\Delta R = 0.3$ and requiring a maximum value of 0.15 on the ratio between the sum of selected tracks momenta and the electron candidate p_{T}.

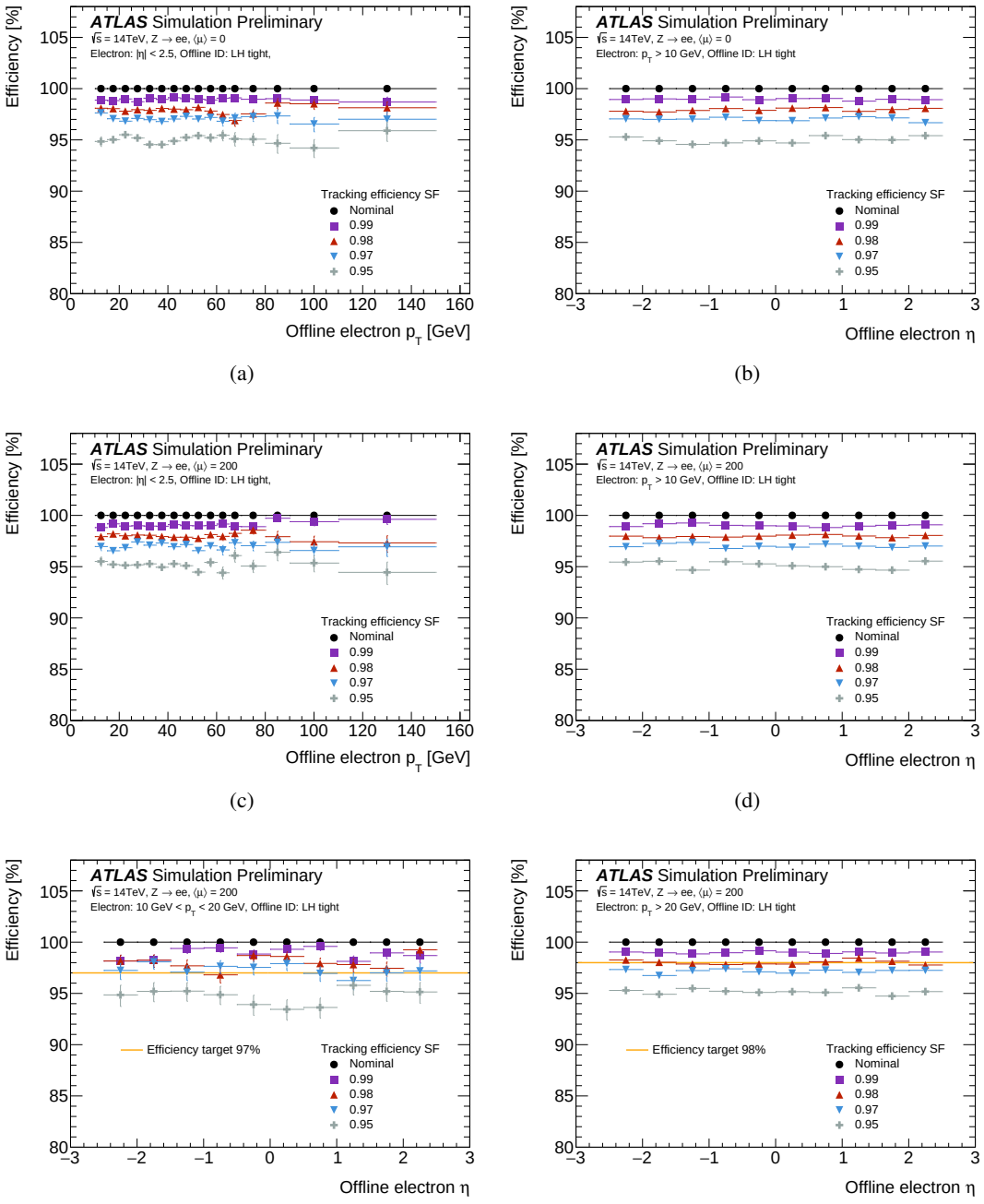

Figure 7: Efficiency of electron reconstruction with different efficiency smearing scale factors applied to GSF tracks on $Z \rightarrow ee$ events, with respect to non isolated offline electrons passing a tight selection. Efficiencies are shown as a function of the offline electron p_{T} and η (a) and (b) with $\langle\mu\rangle = 0$, (c) and (d) with $\langle\mu\rangle = 200$. Efficiency dependency on η (e) for electron p_{T} within 10-20 GeV and (f) for electron p_{T} above 20 GeV, both with $\langle\mu\rangle = 200$. The overlaid orange lines represent possible working points for each p_{T} regime.

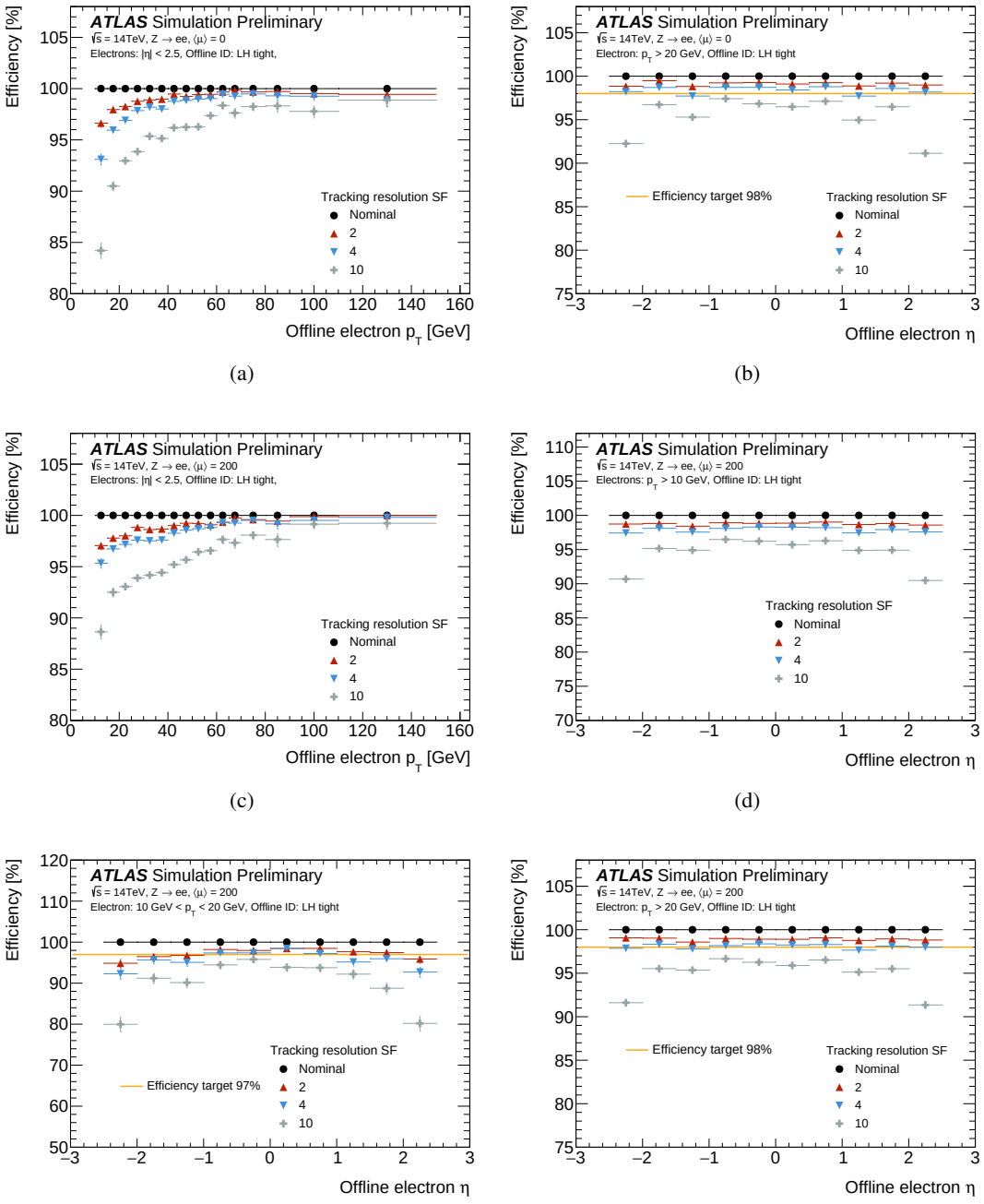

Figure 8: Efficiency of electron reconstruction with different resolution smearing scale factors applied to GSF tracks on $Z \rightarrow ee$ events, with respect to non isolated offline electrons passing a tight selection. Efficiencies are shown as a function of the offline electron p_{T} and η (a) and (b) with $\langle\mu\rangle = 0$, (c) and (d) with $\langle\mu\rangle = 200$. Efficiency dependency on η (e) for electron p_{T} within 10-20 GeV and (f) for electron p_{T} above 20 GeV, both with $\langle\mu\rangle = 200$. The overlaid orange lines represent possible working points for each p_{T} regime.

The efficiency of finding such isolated electrons is shown in Figures 9 and 10, for both reduced efficiency and reduced resolution scenarios, respectively. As already noticed for other single lepton signatures, tracking inefficiency brings the same amount of inefficiency in the identification algorithms, with no evident substructures, also when isolation is applied. The worsening of the momentum resolution affects the electron identification largely at low-momentum and large η, a trend that follows the structure of the resolution smearing functions, and it is critically affected with regard to ATLAS desired physics performance when the resolution is more than 2 or 3 times worse than the offline values. This proves the robustness of the chosen electron identification criteria as a function of the tracking performance, also with high pile-up conditions.

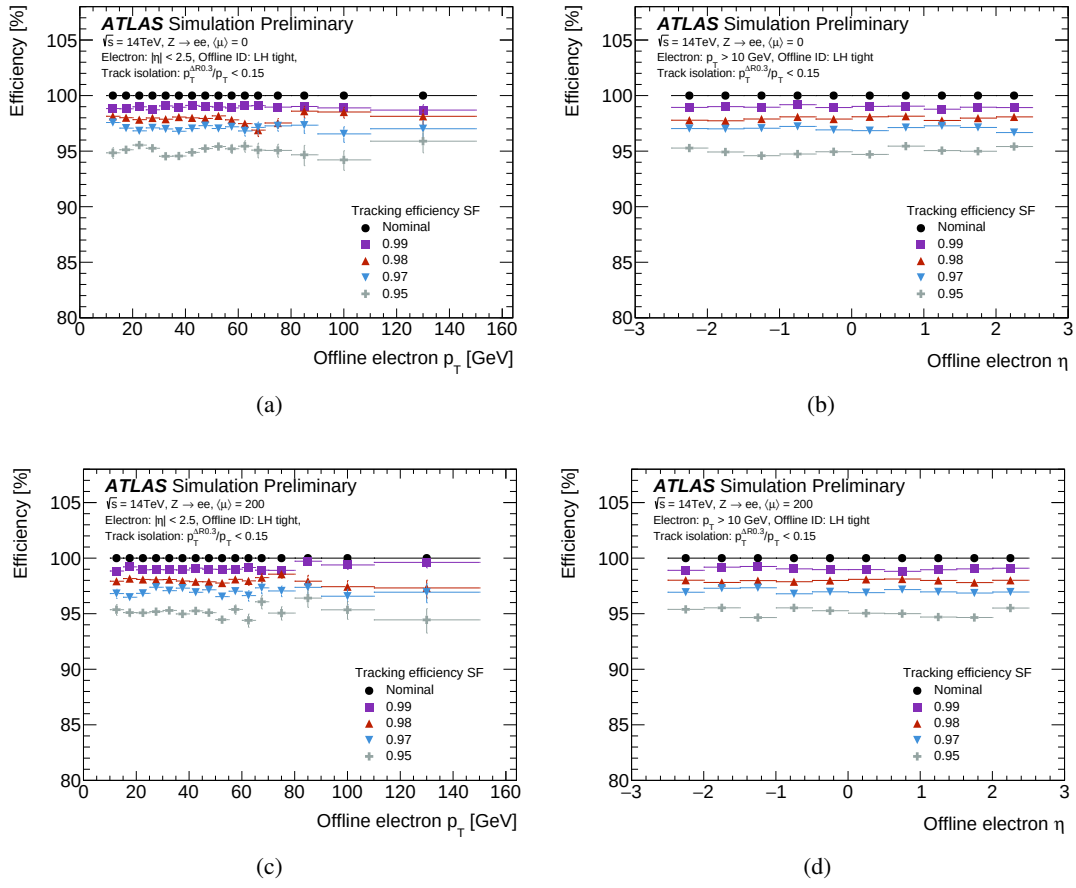

Figure 9: Efficiency trends measured with respect to offline electrons passing the tight electron identification, including isolation, on $Z \rightarrow ee$ events with different efficiency smearing scale factors applied to GSF tracks, shown versus p_{T} and η: (a) and (b) with $\langle\mu\rangle = 0$, (c) and (d) with $\langle\mu\rangle = 200$. Isolation is applied to tight reconstructed electrons, requiring that the sum of the track p_{T} in a cone with maximum $\Delta R = 0.3$ is less than 0.15 of the electron momentum.

5.3 Tau trigger selections

The representative trigger menu summarized in Table 1 includes a 150 GeV single τ trigger and a 40/30 GeV di-τ trigger. These studies focus on the identification of the visible component of a hadronically

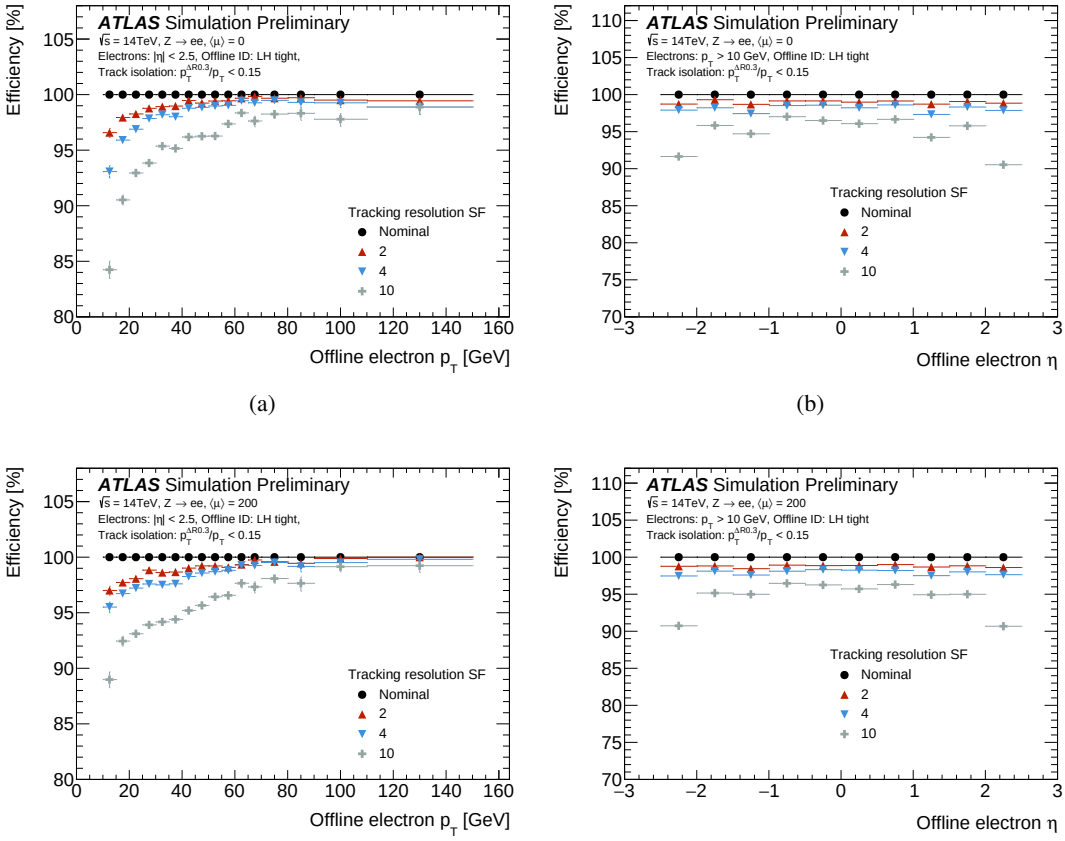

Figure 10: Efficiency trends measured with respect to offline for the tight electron identification, including isolation, on $Z \rightarrow ee$ events with different resolution smearing scale factors applied to GSF tracks, shown versus p_{T} and η: (a) and (b) with $\langle\mu\rangle = 0$, (c) and (d) with $\langle\mu\rangle = 200$. Isolation is applied to tight reconstructed electrons, requiring that the sum of the track p_{T} in a cone with maximum $\Delta R = 0.3$ is less than 0.15 of the electron momentum.

decaying τ lepton ($\tau_{\text{had-vis}}$), which relies on tracks for both the decays to one and three charged pions (one or three-prong) [18]. Two main samples are considered:

- $HH \rightarrow b\bar{b}\tau^{+}\tau^{-}$ events, providing a source of signal $\tau_{\text{had-vis}}$ for efficiency studies;
- di-jet events, used to extract the rejection against QCD background.

The $\tau_{\text{had-vis}}$ selection at Level-0 is based on jets reconstructed with calorimeter topological clusters with hadronic calibration (LC) [19, 20], with a corresponding rate of 200 kHz and adopt the regional tracking option at the EF to achieve early rate rejection through the track association and track counting steps.

The emulation of the Level-0 τ selection is done by requiring the LC-jet seeding the tau candidate to have $p_{\mathrm{T}} > 30$ GeV. After creating the seed-jet, online tau reconstruction and identification consists of the following steps:

- τ tracking: a tracking algorithm is run within a specified RoI around the seed-jet;

- track-to-vertex association: tracks are retained if they pass matching criteria; some of them are described below;
- τ identification: based on track information, the charge and number of prongs (prong-ness) of the $\tau_{\text{had-vis}}$ candidate are derived; a final step distinguishes between taus and jets using tracking and calorimeter information.

This study focuses on two algorithms for track-to-vertex association: one that adopts cuts on reconstructed parameters, and one based on a neural network (NN) approach. The cut-based approach is similar to the current algorithm used for tau track-to-vertex association in the Run 3 trigger [18]. The NN approach, based on the current offline algorithm implementation, classifies tracks as belonging to the seed-jet or another object and is a candidate to replace or improve online track-to-vertex association.

Given the above described selection strategy, these studies focus on the effect of duplicated and fake tracks, and on reduced tracking efficiency and degraded track p_{T} resolution scenarios, all affecting the amount of tracks considered, a critical parameter for the $\tau_{\text{had-vis}}$ identification. To provide a reference for studying the impact of tracking performance on the $\tau_{\text{had-vis}}$ trigger selection, the typical working point adopted in Run 3 for hadronic multi-prong tau triggers is designed to grant an identification efficiency around 82%. The following sections cover the performance of the track-to-vertex association and of the NN track classification and "prong-ness" identification steps, respectively.

5.3.1 Tau track-to-vertex association studies

The τ track-to-vertex association is performed for tracks inside the jet cone under study, as described in Section 4.1 of [18]. Track parameters are recalculated with respect to the candidate τ vertex and tracks are associated to the jet if:

- they lie in a cone of $\Delta R < 0.25$ around the jet seed, or if they satisfy a ghost-particle association technique in the annulus $0.25 < \Delta R < 0.4$ around the seed jet;
- their longitudinal impact parameter z_0, evaluated with respect to the candidate vertex using the τ vertex association algorithm (TJVA), is within a given range (typically 2, 5 or 10 mm).

The distribution of the number of tracks passing the emulated Level-0 selection is shown in Figure 11, comparing signal and background events for different resolution degradation scenarios and with different track p_{T} and z_0 cuts applied.

The rejection against di-jet events can be measured as a function of the efficiency to select true τ candidates, as shown in Figure 12, applying different cuts on the maximum number of tracks in the cone. These results show that for an efficiency around 80% a rejection factor between 3 and 4 can be achieved, and that varying the resolution on track p_{T} leads to the largest effects on the selection.

To derive a figure of merit for the stability of vertex-associated track multiplicity in different performance degradation scenarios, an upper threshold on the number of tracks is defined so that it retains at least 82% of the signal, $N_{\text{tracks}}^{(82)}$. This target efficiency is extracted from the scenarios studied in the TDAQ TDR [6] for an online $\tau_{\text{had-vis}}$ selection using tracks, and also reflects the working points for tau-triggers in Run 3. Based on this cut, more variables can be evaluated, providing insight on the distributions of track multiplicity N_{tracks} for signal and background:

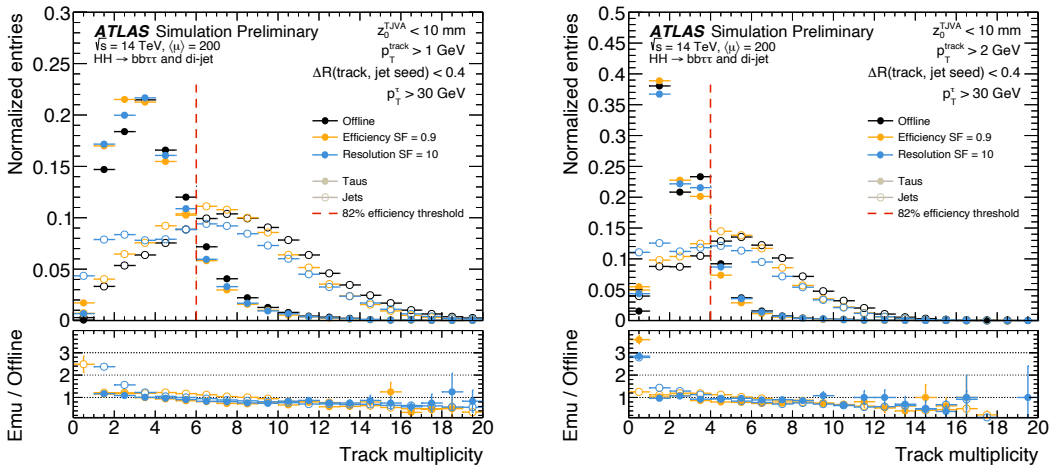

(a) (b)

Figure 11: Number of tracks associated to a true τ candidate, for both signal ($HH \rightarrow b\bar{b}\tau^+\tau^-$) and background (di-jet) events with $\langle\mu\rangle$=200. For τ candidates with p_T > 30 GeV, tracks with p_T > 1 GeV in (a) and p_T > 2 GeV in (b) are requested with z_0 cuts at 10 mm and ΔR cuts at 0.4 applied. For each case, different performance degradation scenarios are explored and bottom panels represent the ratio between the given scenario and the nominal case. The red dashed line indicates the track multiplicity cut that preserves at least 82% of the signal events.

- the efficiency on signal and the rejection on background for the request $N_{\text{tracks}} < N_{\text{tracks}}^{(82)}$; these quantities are related to the possibly different way in which signal and background multiplicities can be affected by tracking degradation scenarios;
- the difference, on signal events, between the average number of tracks, $\langle N_{\text{tracks}}\rangle$, and the $N_{\text{tracks}}^{(82)}$ cut; this provides a test of the shape stability of the multiplicity for signal events and a rough estimate of the number of additional tracks considered for each true τ candidate.

These variables are shown for different tracking performance variations in Table 2, for both global and regional tracking options, that also imply a different cut on track p_T. In both cases, they prove to be stable as a function of the emulated tracking efficiency, track momentum resolution, and z_0 cut.

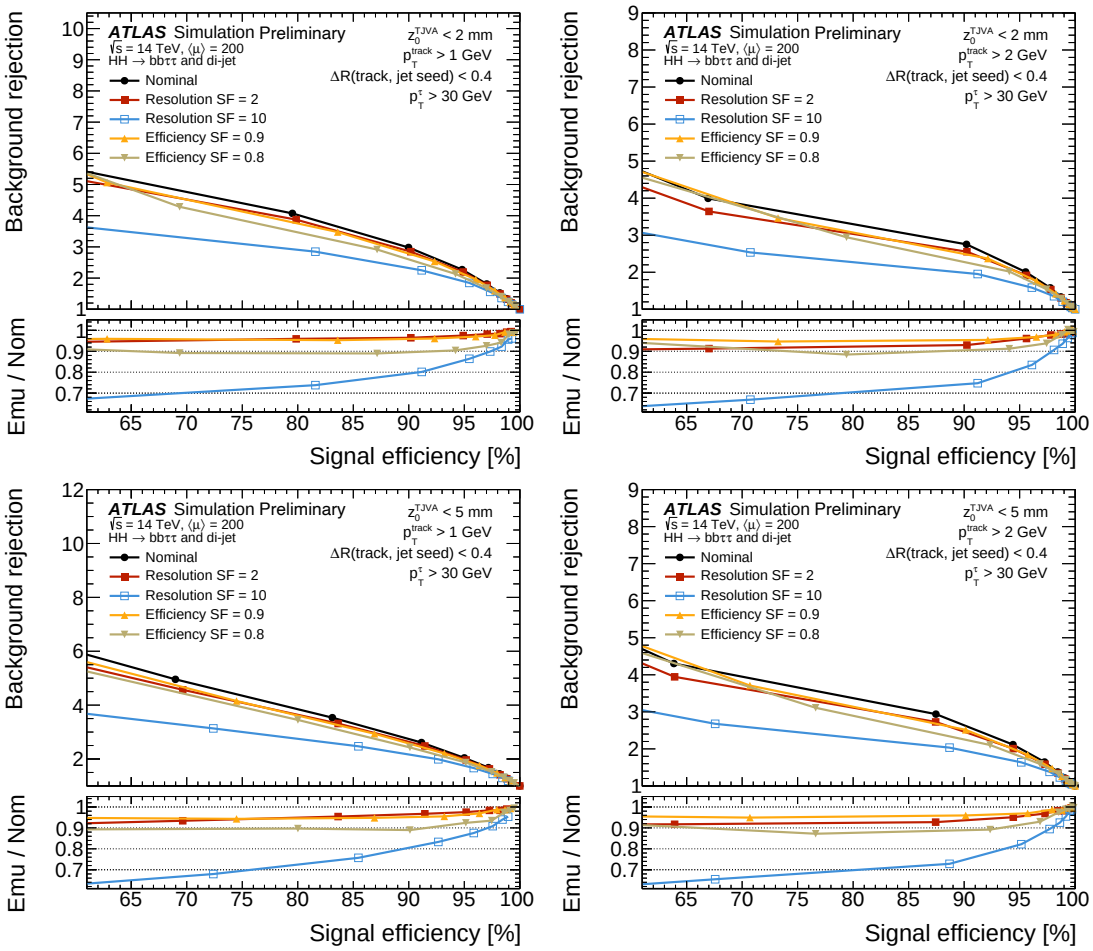

Figure 12: Efficiency on $HH \to b\bar{b}\tau^+\tau^-$ versus background rejection on di-jet events with $\langle\mu\rangle$=200, as a function of the cut on the maximum total number of tracks associated to a τ candidate. For τ candidates with $p_{\mathrm{T}} > 30$ GeV, tracks are counted if they pass a ΔR cut applied at 0.4, a z_0 cut applied at 2 mm (top) and 5 mm (bottom), and having $p_{\mathrm{T}} > 1$ GeV (left) and $p_{\mathrm{T}} > 2$ GeV (right). For each case, different performance degradation scenarios are explored. The ratio is calculated by extrapolating the nominal curve to each emulated point.

Table 2: Variables related to vertex-associated track multiplicity in τ candidates, for different tracking performance scenarios: nominal, tracking efficiency scale factor 0.9 and 0.8, scale factor 2 and 10 on track p_{T} resolution. Results are shown for three different z_0 cuts (2, 5, and 10 mm), and with track $p_{\mathrm{T}} > 1$ GeV and $p_{\mathrm{T}} > 2$ GeV requirement, emulating respectively the global and the regional tracking setup. For each scenario are shown: the (rounded) cut on the track multiplicity that preserves 82% of the signal events, $N_{\mathrm{tracks}}^{(82)}$; the average number of tracks associated, $\langle N_{\mathrm{tracks}} \rangle$ and their difference; the resulting efficiency and background rejection at the $N_{\mathrm{tracks}}^{(82)}$ cut.

track $p_{\mathrm{T}} > 1$ GeV (global tracking)															
	nominal			efficiency SF = 0.9			efficiency SF = 0.8			p_{T} res. SF = 2			p_{T} res. SF = 10		
max. track z_0 [mm]	2	5	10	2	5	10	2	5	10	2	5	10	2	5	10
$N_{\mathrm{tracks}}^{(82)}$	5	5	6	4	5	6	4	5	5	5	5	6	5	5	6
$\langle N_{\mathrm{tracks}} \rangle$	2.5	3.0	3.7	2.3	2.7	3.3	2.0	2.4	3.0	2.5	3.0	3.6	2.4	2.8	3.4
$N_{\mathrm{tracks}}^{(82)} - \langle N_{\mathrm{tracks}} \rangle$	2.5	2.0	2.3	1.7	2.3	2.7	2.0	2.6	2.1	2.5	2.0	2.4	2.6	2.2	2.6
eff. $N_{\mathrm{tracks}}^{(82)}$ cut [%]	90	83	83	84	87	87	87	90	83	90	84	84	91	85	86
rej. $N_{\mathrm{tracks}}^{(82)}$ cut	3.0	3.5	3.2	3.5	2.9	2.6	2.9	2.4	2.9	2.8	3.3	2.9	2.3	2.5	2.2

track $p_{\mathrm{T}} > 2$ GeV (regional tracking)															
	nominal			90% efficiency			80% efficiency			p_{T} res. SF = 2			p_{T} res. SF = 10		
max. track z_0 [mm]	2	5	10	2	5	10	2	5	10	2	5	10	2	5	10
$N_{\mathrm{tracks}}^{(82)}$	4	4	4	4	4	4	4	4	4	4	4	4	4	4	4
$\langle N_{\mathrm{tracks}} \rangle$	2.0	2.2	2.3	1.8	1.9	2.1	1.6	1.7	1.8	2.0	2.1	2.3	1.9	2.0	2.2
$N_{\mathrm{tracks}}^{(82)} - \langle N_{\mathrm{tracks}} \rangle$	2.0	1.9	1.7	2.2	2.1	1.9	2.4	2.3	0.0	2.0	1.9	1.7	2.1	2.0	1.8
eff. $N_{\mathrm{tracks}}^{(82)}$ cut [%]	90	87	84	92	90	87	94	92	90	90	87	84	91	89	85
rej. $N_{\mathrm{tracks}}^{(82)}$ cut [%]	2.8	2.9	3.1	2.4	2.5	2.6	2.0	2.1	2.2	2.6	2.7	3.0	2.0	2.0	2.1

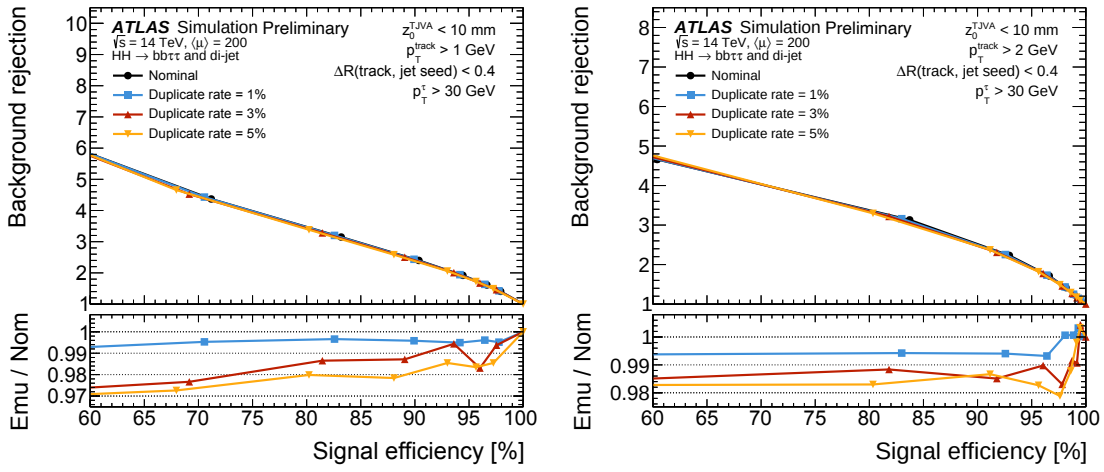

(a) (b)

Figure 13: Efficiency on $HH \to b\bar{b}\tau^+\tau^-$ versus background rejection on di-jet events with $\langle\mu\rangle$=200, as a function of the cut on the maximum total number of tracks associated to a τ candidate. For τ candidates with $p_{\mathrm{T}} > 30$ GeV, tracks are counted if they pass a z_0 cut applied at 10 mm, a ΔR cut applied at 0.4, and have $p_{\mathrm{T}} > 1$ GeV in (a) and > 2 GeV in (b). For each case, different track duplication rates are explored. The ratio is calculated by extrapolating the nominal curve to each emulated point.

Table 3: Variables related to vertex-associated track multiplicity in τ candidates, for different duplicate track rate. Results are shown for a track requirement of $p_{\mathrm{T}} > 1$ GeV (to emulate global tracking) and $p_{\mathrm{T}} > 2$ GeV (to emulate regional tracking), and with $z_0 < 10$ mm. For each scenario are shown: the (rounded) cut on the track multiplicity that preserves 82% of the signal events, $N_{\mathrm{tracks}}^{(82)}$; the resulting efficiency and background rejection at the $N_{\mathrm{tracks}}^{(82)}$ cut, and their product.

track $p_{\mathrm{T}} > 1$ GeV (global tracking)						
duplicate rate	nominal	0.1%	0.5%	1%	3%	5%
$N_{\mathrm{tracks}}^{(82)}$	6	6	6	6	7	7
efficiency of $N_{\mathrm{tracks}}^{(82)}$ cut	83%	83%	83%	83%	89%	88%
rejection of $N_{\mathrm{tracks}}^{(82)}$ cut	3.15	3.15	3.17	3.20	2.50	2.58
eff. $\times$ rej. $N_{\mathrm{tracks}}^{(82)}$ cut	2.6	2.6	2.6	2.7	2.2	2.3
track $p_{\mathrm{T}} > 2$ GeV (regional tracking)						
duplicate rate	nominal	0.1%	0.5%	1%	3%	5%
$N_{\mathrm{tracks}}^{(82)}$	4	4	4	4	5	5
efficiency of $N_{\mathrm{tracks}}^{(82)}$ cut	84%	84%	83%	83%	92%	91%
rejection of $N_{\mathrm{tracks}}^{(82)}$ cut	3.13	3.13	3.15	3.16	2.31	2.37
eff. $\times$ rej. $N_{\mathrm{tracks}}^{(82)}$ cut	2.6	2.6	2.6	2.6	2.1	2.2

In addition, the effects from different track multiplicities are studied through the emulation of the track duplication, described in 4.1. Different track duplication rates are applied to check the stability of the track multiplicity selection. As shown in Figure 13, the contribution of fake tracks decreases the efficiency linearly, but roughly maintains the efficiency vs. rejection curve. For each track duplication rate scenario, a $N_{\mathrm{tracks}}^{(82)}$ cut is also defined and its signal efficiency and background rejection are evaluated. To mitigate rounding fluctuations related to the non-continuous nature of the cut, an additional figure of merit is defined as the product of the background rejection and the signal efficiency. These variables are shown in Table 3, for both global and regional tracking. The product of efficiency and rejection for the $N_{\mathrm{tracks}}^{(82)}$ cut is demonstrated to be stable up to 1% duplicate rate, after which a more significant drop is observed. This figure of merit is relatively constant as a function of the z_0 cut and is stable across efficiency and resolution degradation, which indicates that the resolution is not setting constraints on this factor.

5.3.2 Tau track classification

The scope of the τ track classification is to assign and count tracks in a cone around the candidate calorimeter jet seed. The initial track selection is made with a track classification algorithm, based on a recurrent neural network model (RNN). This algorithm is able to identify τ tracks, separating them from those produced in pile-up collisions, photon conversions and other particles resulting from the hard scatter. The track variables used as input for this algorithm include p_{T} and η, in addition to quantities related to the number of hits on the track.

Based on the number of tracks classified as coming from the τ-lepton, the RNN can be used to identify the "prong-ness" of the τ candidate; this determines the choice of the τ identification tuning to be adopted for the corresponding candidate. The τ identification algorithm has three tunes: zero-prong, one-prong, and multi-prong, the latter taking two- and three-prong τ candidates. Each tune of the τ identification algorithm

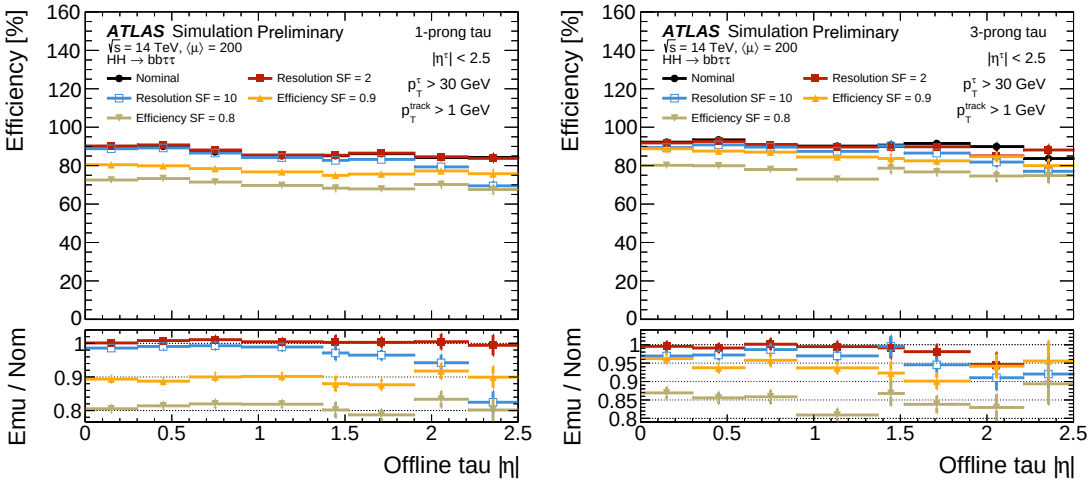

(a) (b)

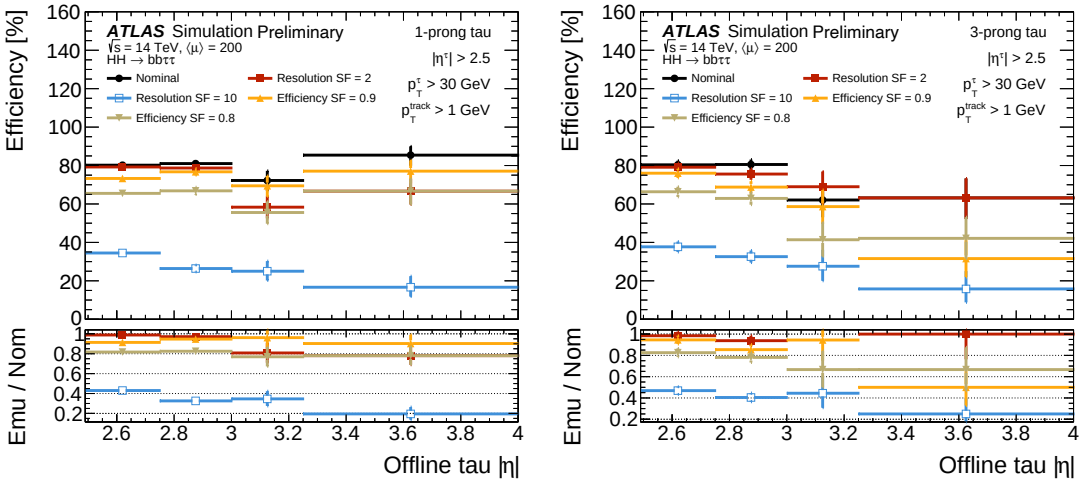

(c) (d)

Figure 14: Efficiency to correctly identify the "prong-ness" of $\tau_{\text{had-vis}}$ candidates on $HH \to b\bar{b}\tau^+\tau^-$ events with $\langle\mu\rangle$ = 200, as a function of η for (a) central 1-prong τs; (b) central 3-prong τs; (c) forward 1-prong τs; (d) forward 3-prong τs; results are shown for different tracking performance degradation scenarios. Only tracks with p_{T} >1 GeV within τ candidates with p_{T} >30 GeV are counted.

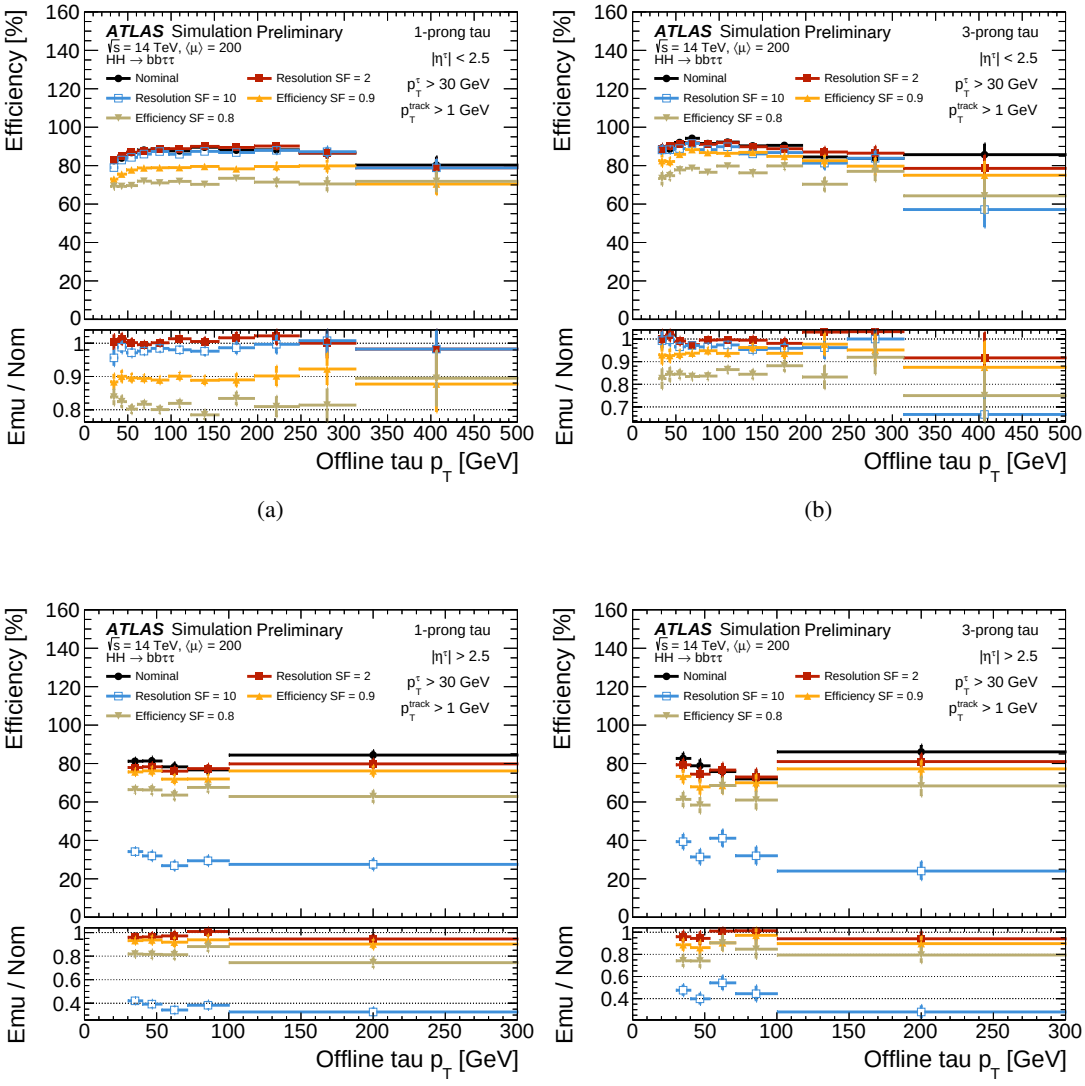

Figure 15: Efficiency to correctly identify the "prong-ness" of $\tau_{\text{had-vis}}$ candidates on $HH \to b\bar{b}\tau^+\tau^-$ events with $\langle\mu\rangle$ = 200, as a function of p_{T} for (a) central 1-prong τs; (b) central 3-prong τs; (c) forward 1-prong τs; (d) forward 3-prong τs; results are shown for different tracking performance degradation scenarios. Only tracks with p_{T} >1 GeV within τ candidates with p_{T} >30 GeV are counted.

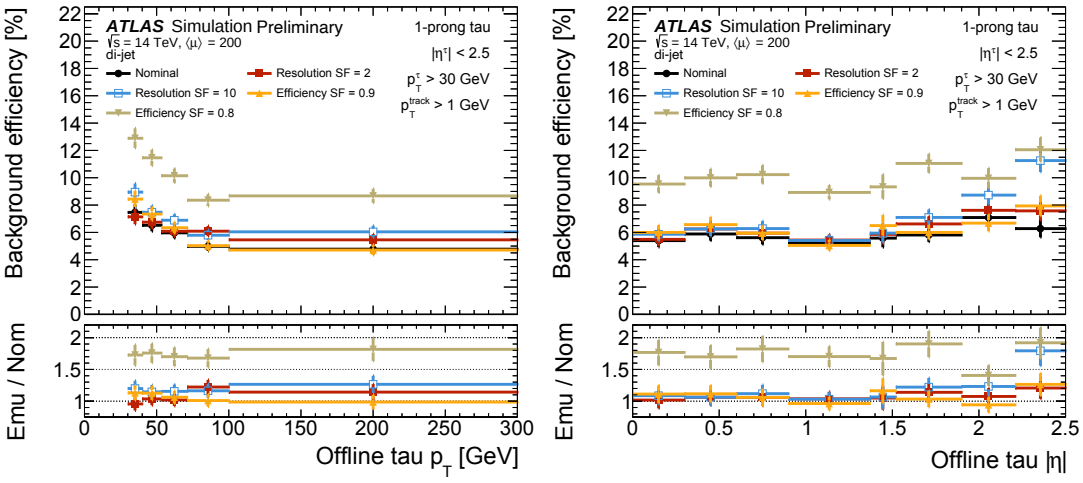

(a) (b)

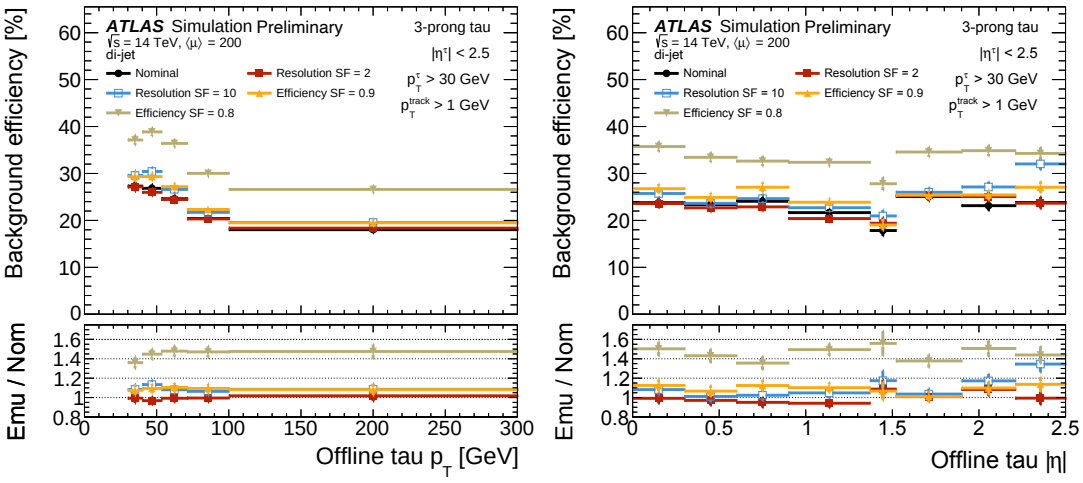

(c) (d)

Figure 16: Probability to incorrectly identify a QCD jet as a τ-lepton, measured on background events at $\langle\mu\rangle$=200 as a function of p_{T} and η for central τ candidates: (a) (b) 1-prong τs; (c) (d) 3-prong τs; results are shown for different tracking performance degradation scenarios. Only tracks with p_{T} >1 GeV within τ candidates with p_{T} >30 GeV are counted.

requires different input variables, resulting in poor performance for candidates tagged with the wrong tuning. For that reason, the track classification task plays a crucial role in ensuring good identification efficiency and separation from jets. The zero-prong tune is significantly less efficient than the other two tunes, therefore τ candidates falling into the zero-prong category are counted as incorrectly identified in this work.

This study uses emulated EF Tracking tracks to train and test the track classification algorithm, without any change in the remaining $\tau_{\text{had-vis}}$ identification chain. The central ($|\eta| < 2.5$) and forward ($2.5 < |\eta| < 4$) regions are studied and trained separately, to improve forward performance.Two sets of samples are adopted:

- the training is performed on $\gamma^* \rightarrow \tau\tau$ and QCD events;
- classification performance is evaluated on signal $HH \rightarrow b\bar{b}\tau^+\tau^-$ events.

The training is performed on τ leptons with $p_{\text{T}} > 15$ GeV associated to jet seeds with $p_{\text{T}} > 5$ GeV. A maximum of 15 tracks associated to the seed-jet, sorted by p_{T}, are considered. The tau candidates used for training are separated into central and forward samples, resulting in less candidates for training the forward classifier than the central. The τ identification performance is studied for different EF Tracking efficiency and p_{T} resolution degradation scenarios, the latter being a key ingredient for a correct track classification. Two main undesired effects are expected, namely the reduction of the average track p_{T} and of the track multiplicity. For each performance degradation scenario, the RNN is retrained; preliminary studies demonstrated that, while ineffective in recovering tracking inefficiencies, this proves crucial to compensate reduced p_{T} resolution. The compensation for reduced p_{T} resolution is worse for the forward track classifier, likely due to less tau candidates in its training.

Starting from the individual track classification efficiency, measuring the probability to correctly identify a τ track, a more relevant figure of merit can be defined for each τ candidate, measuring the probability of correctly identifying the "prong-ness" of its decay. Figures 14 show this efficiency as a function of η for both central and forward taus, in both 1- and 3-prong decays. These plots demonstrate that the performance in the forward region is more sensitive to a possible resolution degradation than the central region. The plots in Figure 15 show the same results as a function of p_{T}. While the classifier is trained to have a flat efficiency in p_{T}, the per-tau efficiency, calculated with respect to the true "prong-ness", includes also inefficiencies in resolving individual tracks, in particular at large p_{T} where tracks tend to overlap. In the forward region, the increase of efficiency at large p_{T} is proven to be dependent on the signal and efficiency definition, and is still under study.

The efficiency on background, defined as the probability to incorrectly identify QCD jets as τ candidates, is shown in Figure 16, for all categories and regions. The reduced tracking efficiency and degraded p_{T} resolution are shown to increase the efficiency on non-tau jets, thus reducing the rejection power.

5.4 Jets and multi-jets trigger selections

The representative trigger menu summarized in Table 1 includes a 4-jet trigger, for important signals such as $HH \rightarrow 4b$. Jets from pile-up collisions can mimic the signal selection and increase the rates to unmanageable levels. The selection on the jet multiplicity can either select the target hard QCD process from a single process, or randomly combine jets from different pp collision vertices. At low jet momentum, the latter mechanism is dominant, because of the abundance of low-p_{T} pile-up jets.

The Level-0 multi-jet selection makes use of the calorimeter information only, not granting an optimal pile-up mitigation. The EF Tracking reconstruction is then used to associate tracks to jets and to impose requirements on their impact parameter z_0. This allows events with four jets stemming from the hard-scatter vertex to be distinguished from events with random overlapping di-jet pairs generated from different vertices.

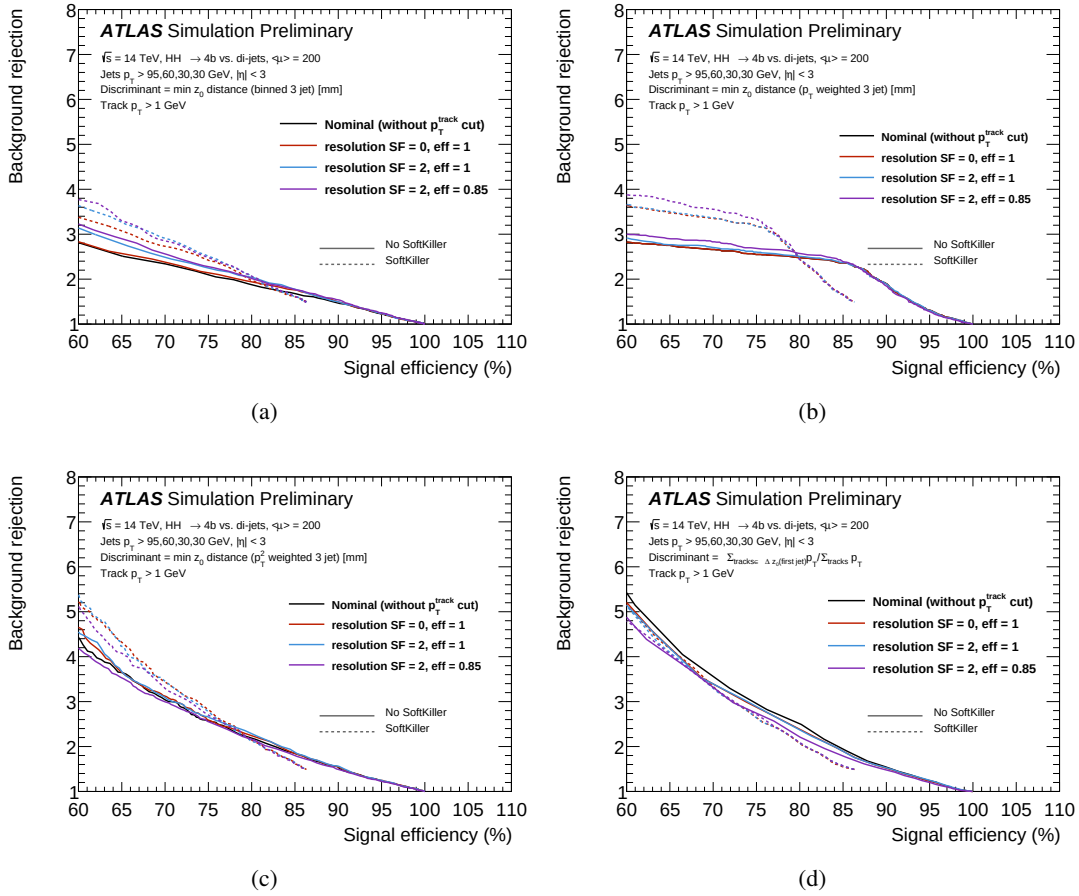

Figure 17: Signal acceptance for $HH \rightarrow 4b$ versus background acceptance, with respect to the emulated Level-0 EM topological jet selection, corresponding to different multi-jet common vertex discriminants, for different tracking degradation scenarios, with and without SoftKiller [21]; the discriminants, described in detail in the main text are: (a) minimum distance between z_0 averages; (b) minimum distance between z_0 p_{T}-weighted averages; (c) minimum distance between z_0 ${p_{\mathrm{T}}}^2$-weighted averages; (d) normalized $\sum \vec{p}_{\mathrm{T}}$ for tracks within 5 mm of the leading jet's z_0 average.

To study the performance of multi-jet triggers, two main samples are considered:

- $HH \rightarrow 4b$ events, as signal benchmark signature for the HL-LHC;
- di-jet and fully hadronic $t\bar{t}$ events, used as background samples.

The Level-0 calorimeter trigger is emulated starting from offline jets built as clusters of topologically-connected energy depositions in the calorimeters (called topo-clusters) [19], as foreseen in Run 4. For this study, the multi-jet item was defined requiring four jets to fall within $|\eta| < 3$ and to have respectively p_{T}

greater than 95, 60, 30 and again 30 GeV; these asymmetric Level-0 thresholds have been optimized with dedicated studies, as mentioned in Ref. [14].

Emulated EF Tracking tracks, both in regional and full-scan scenarios, are then matched to jets within a cone of $\Delta R < 0.4$. In this analysis, topo-cluster jets with energy defined at the electromagnetic scale [22] have been adopted, for the sake of simplicity; it is expected that the more sophisticated particle-flow jet reconstruction approach will be used in the Run 4 EF trigger, but as already stated, in these studies we neglect it because still under commissioning. Likewise, the study of the impact of the quality of the tracks on the jet calibration is outside the scope of this study, and is neglected essentially assuming that the energy response/resolution for the jets is unchanged in the different scenarios. The performance estimated in this study are then to be considered optimistic.

Building on these ingredients, different algorithms can be used to reject multi-jet background. Some of them, like SoftKiller [21], are applying a purely calorimeter-based pile-up suppression. Other algorithms have been developed taking advantage of the tracking information, like for example:

- a fast vertexing algorithm, designed for firmware implementation in FPGAs, originally proposed and studied in Ref. [14]; this is based on the idea of binning the z_0 of the tracks from each jet, and calculating the minimum bin width that contains tracks from at least three of the four jets, considered as a proxy for the minimum distance between the jets' origins along the beam axis;
- DIPZ, a Deep Set [23] based algorithm for predicting the z_0 and $\sigma(z_0)$ of a jet from its constituent tracks;
- vertex-based pile-up suppression using JVT [24].

Simplified approaches, or even emulations of these algorithms have been studied and results are reported in the following sections.

5.4.1 Simple multi-jet vertexing algorithm

Inspired by the fast vertexing algorithm in Ref. [14], four different algorithms have been studied, based on discriminant variables related to the distance among jets along the beam axis. The following metrics have been explored:

- minimum distance in z_0 between tracks from 3 of the leading 4 p_{T} jets;
- minimum distance between p_{T}-weighted mean z_0 for 3 of the leading 4 p_{T} jets;
- $\sum \vec{p}_{\mathrm{T}}$ for tracks within 5 mm in z_0 of the leading p_{T} jet, normalized to the total $\sum \vec{p}_{\mathrm{T}}$ for the leading 4 p_{T} jets;
- minimum distance between p_{T}^2-weighted mean z_0 for 3 of the leading 4 p_{T} jets.

The performance of these algorithms has been studied with and without applying `SoftKiller` on top of them. Figure 17 shows the background rejection for jets selected at Level-0 as a function of signal efficiency, measured with respect to truth jet, for all studied algorithms. Results are reported for various tracking performance degradation scenarios and compared with the nominal regional scenario, which reconstructs only tracks with at least $p_{\mathrm{T}} > 1$ GeV. All the algorithms prove quite robust to track degradation and, in many cases, the adoption of Softkiller is found not to have a significant impact on performance.

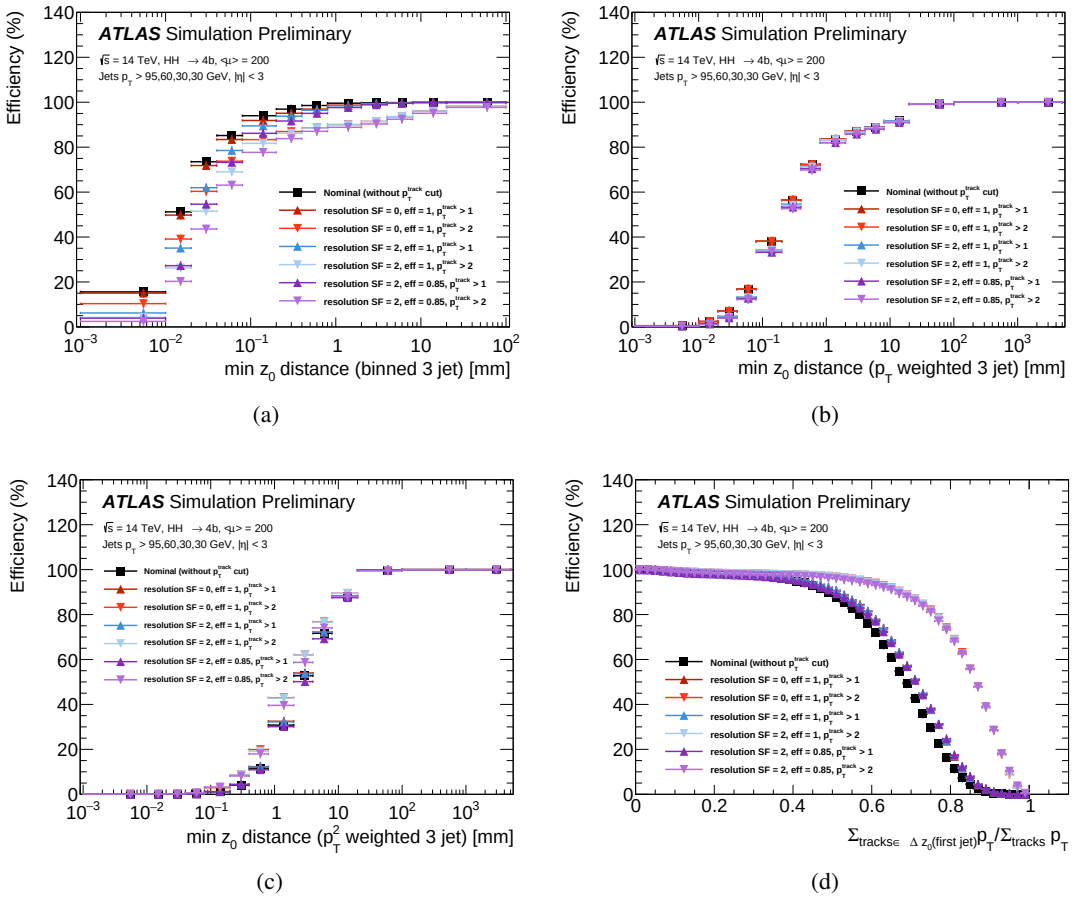

(a) (b)

(c) (d)

Figure 18: Efficiency on signal $HH \rightarrow 4b$ with respect to the emulated Level-0 EM topological jet selection, for the four different multi-jet common vertex discriminants, with different track degradation scenarios; the discriminants, described in detail in the main text are: (a) minimum distance between z_0 averages; (b) minimum distance between z_0 p_{T}-weighted averages; (c) minimum distance between z_0 p_{T} ^{2}-weighted averages; (d) normalized $\sum \vec{p}_{\mathrm{T}}$ for tracks within 5 mm of the leading jet's z_0 average.

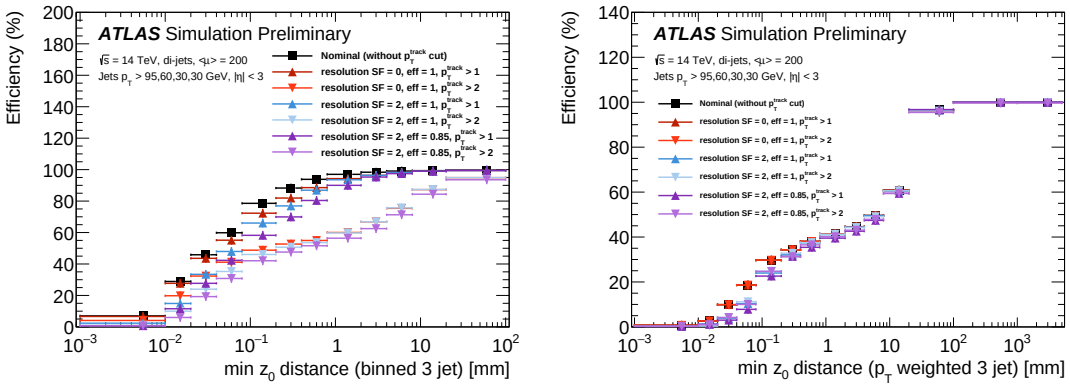

(a) (b)

(c) (d)

Figure 19: Di-jet background efficiency with respect to the emulated Level-0 EM topological jet selection, for the four different multi-jet common vertex discriminants, with different track degradation scenarios; the discriminants, described in detail in the main text are: (a) minimum distance between z_0 averages; (b) minimum distance between z_0 p_{T}-weighted averages; (c) minimum distance between z_0 p_{T} ^{2}-weighted averages; (d) normalized $\sum \vec{p}_{\mathrm{T}}$ for tracks within 5 mm of the leading jet's z_0 average.

The ROC curves described above are derived from the efficiency measurement on both $HH \rightarrow 4b$ signal events and on di-jet background events. For completeness, they are shown as a function of the selection parameter respectively in Figures 18 and 19 (without SoftKiller only).

5.4.2 Neural-network multi-jet algorithm

In order to emulate the performance of more sophisticated algorithms, a neural network classifier based on a `DeepSets` architecture [25] has been also studied. It was trained to separate di-jet events from $HH \rightarrow 4b$ events, taking as input the kinematic information of the leading eight jets (jet p_{T}, η, ϕ, invariant mass, track multiplicity) as well as the kinematics and vertex information for the two leading tracks within $\Delta R < 0.4$ of each jet (track p_{T}, η, ϕ, z_0, d_0, $\sigma(z_0)$, $\sigma(d_0)$, q/p, $z_0/\sigma(z_0)$, $d_0/\sigma(d_0)$).

The efficiency versus rejection curves obtained with this algorithm, for different tracking degradation scenarios, are reported in Figure 20. It shows that a simple ML classifier can significantly improve the multi-jet identification with respect to the simple algorithm presented in Section 5.4.1, paying the price of an increased sensitivity to the tracking performance. Dedicated retraining of the simple ML classifier using the most pessimistic degraded scenario is able to greatly reduce this sensitivity. A careful scrutiny of systematic effects when applied to physics analyses will be anyway required for this approach.

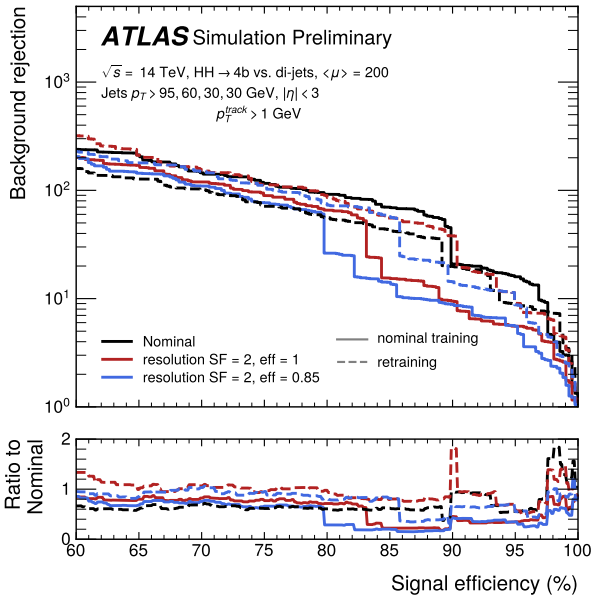

Figure 20: Signal acceptance for $HH \rightarrow 4b$ versus background acceptance, with respect to the emulated Level-0 EM topological jet selection, for a simplified neural network algorithm based on `DeepSets`, taking as input the kinematic information of the leading eight jets and the two leading tracks within a $\Delta R < 0.4$ cone of each jet, with track p_{T} above 1 GeV. Both options with and without an additional training with the smeared parameters are shown. The re-training is performed on the sample with resolution SF = 2 and efficiency SF = 0.85.

5.4.3 Vertex-based pile-up suppression algorithm

A simple but powerful discriminant for the association of jets with primary vertices is the $R_{p_{\mathrm{T}}}$ jet variable [24], defined as the scalar sum of the p_{T} of tracks inside the jet cone that pass a selection tagging

them as originating from the hard-scatter vertex (PV_0), divided by the fully calibrated jet p_{T}, i.e.

$$R_{p_{\mathrm{T}}} = \frac{\sum p_{\mathrm{T}}^{\mathrm{track}}(PV_0)}{p_{\mathrm{T}}^{\mathrm{jet}}} \tag{1}$$

Small values of $R_{p_{\mathrm{T}}}$ correspond to jets which have a small fraction of charged-particle p_{T} originating from the hard-scatter vertex PV_0. These jets are therefore likely to be pile-up jets. With high level of pile-up and in the forward region, the power of this discriminant is reduced, because the longitudinal impact parameter resolution becomes worse and the pile-up tracks could have more chance to be incorrectly included in the numerator of $R_{p_{\mathrm{T}}}$.

Results presented in the following adopt a simple track-to-vertex association technique; the p_{T}-weighted z_0 of all tracks in the leading jet is computed and tracks from all jets are tagged as coming from PV_0 if their z_0 is within 5 mm from it. Based on this definition, Figure 21 compares the $R_{p_{\mathrm{T}}}$ distribution in signal and di-jet events, distinguishing jets coming from the hard-scatter interaction and those from pile-up collisions. The efficiency as a function of the cut applied to this variable is shown separately for $HH \rightarrow 4b$ events

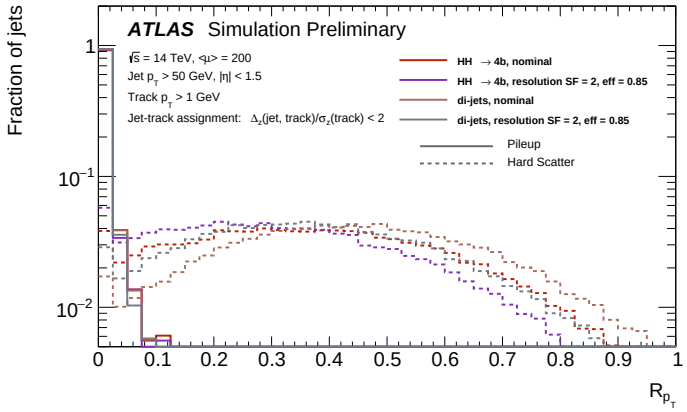

Figure 21: Distribution of the $R_{p_{\mathrm{T}}}$ variable using the track-to-vertex association based on the p_T^2-weighted distance from the leading jet; results are presented for signal $\rightarrow b\bar{b}b\bar{b}$ and background di-jet samples, comparing; different emulated tracking performance scenarios are considered. Only central ($|\eta| < 1.5$) jets are considered in the distributions, but similar trends are seen in other regions as well.

and di-jet events in Figure 22. Different scenarios are considered with varying track p_{T} thresholds, tracks efficiencies, and track resolution SFs. Minimal difference between these scenarios is observed, with the largest degradation in performance coming from a potential loss in track efficiency. Corresponding ROC curves are shown in Figure 23, for the entire jet samples and only for jets passing a selection based on the SoftKiller algorithm.

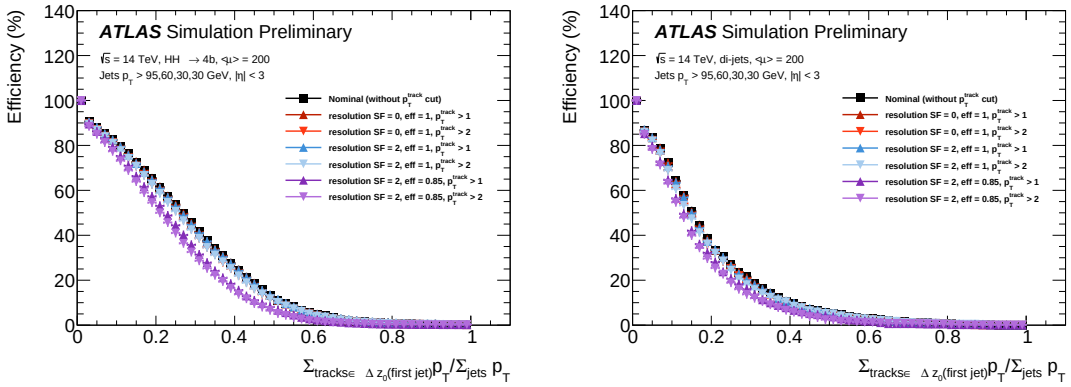

(a) (b)

Figure 22: Efficiency with respect to the emulated Level-0 EM topological jet selection, of a selection based on $R_{p_{\mathrm{T}}}$ calculated with respect of p_T^2-weighted jet tracks vertex, (a) for signal $HH \rightarrow 4b$ and (b) for background di-jet events.

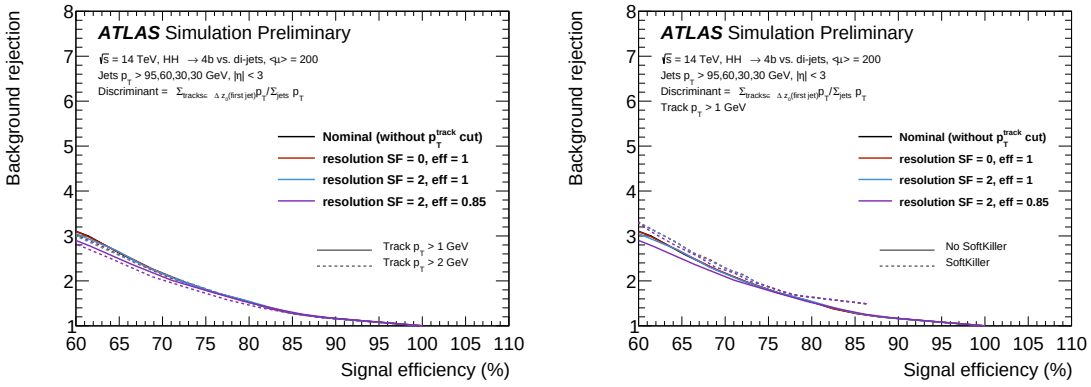

(a) (b)

Figure 23: Signal acceptance for $ZZ \rightarrow 4b$ versus background acceptance, with respect to the emulated Level-0 EM topological jet selection, of a selection based on $R_{p_{\mathrm{T}}}$ calculated with respect of p_T^2-weighted jet tracks vertex. Several scenarios are described, (a) with different track p_{T} cuts and (b) with the addition of SoftKiller.

5.5 Flavour tagging trigger selections

The representative trigger menu summarized in Table 1 includes the baseline heavy-flavour jet trigger targeting $HH \rightarrow b\bar{b}b\bar{b}$ events at the HL-LHC; this requires at least two jets tagged as b-jets (jets containing a B-hadron) on a total of at least 4 jets. The focus of such triggers is on relatively low-p_{T} jets, since events containing very high-p_{T} jets can be selected using jet triggers without any flavour identification.

The menu has been designed assuming that the use of b-tagging can reduce the multi-jet rate from 25 to 0.35 kHz. This choice is based on:

- the typical working point adopted in Run 3 multi-b-jet trigger items, which is designed to grant a 77% b-tagging efficiency, inclusive in jet p_{T} [5];
- the target rejection factor against light jets of 70, as defined by studies in Ref. [2].

The b-jet trigger in Run 3 [26, 27] exploits flavour tagging algorithms developed for physics analysis, optimised for online operation. In particular, for its final selection it is using the GN1 algorithm [28], based on graph neural networks, which shows better c- and light-jet rejection compared with the previous taggers, across the full range of b-jet tagging efficiencies. The offline performance of this tagger has been measured on simulated HL-LHC samples [29]. Recently, an upgraded version of the GN1 tagger, called GN2, has been developed, which adopts an improved training procedure and an optimised transformer architecture [30]. As the GN2 tagger is now becoming the standard for offline reconstruction and shows a better performance than GN1, it has been the focus for these studies.

For each investigated EF Tracking scenario, emulated tracks are used to retrain the GN2 tagger, based on two simulated samples:

- $t\bar{t}$ events, providing a source of jets from beauty, charm and light quarks;
- $Z' \rightarrow q\bar{q}$ events[3], to grant a good identification performance also on high-p_{T} jets.

GN2 performance is then studied on $t\bar{t}$ events, to evaluate the individual b-jet tagging performance; results are evaluated based on the true simulated flavour of jets. The same track quality selection criteria adopted for offline operation are applied. Unless stated differently, all the EF Tracking emulation scenarios include a minimum track p_{T} requirement of 1 GeV, matching the full-scan tracking configuration; this is true also in case no tracking performance degradation is applied, called nominal scenario in the following.
The most crucial track parameters affecting the jet flavour tagging performance are the transverse and longitudinal impact parameters (d_0 and z_0). Figures 24 and 25 respectively show the effect of applying a track resolution scale factor on the d_0 distributions and on the signed d_0 and z_0 significance, defined as the ratio between the impact parameter of a track and the estimated error in it. The plots distinguish the performance in the forward ($|\eta| > 2$) and in the central regions ($|\eta| < 2$).

[3] In these samples, the BSM Z' boson is constructed in such a manner that it produces a relatively flat jet p_{T} spectrum up to 5 TeV and decays to an equal numbers of b-, c- and light-jets.

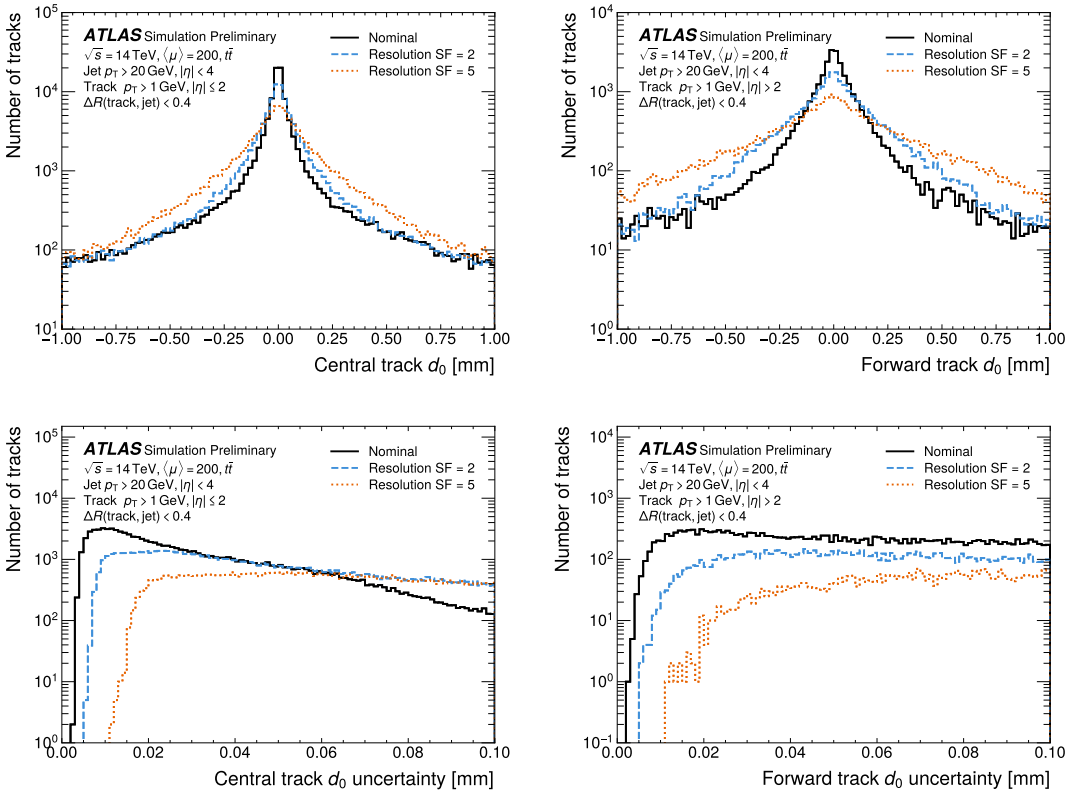

Figure 24: Distributions of the track d_0 (top) and d_0 uncertainty (bottom) for tracks associated to jets in the simulated $t\bar{t}$ events that are used for training the b-tagging algorithm, in the central (left) and forward (right) regions, as a function of different track resolution degradation scenarios.

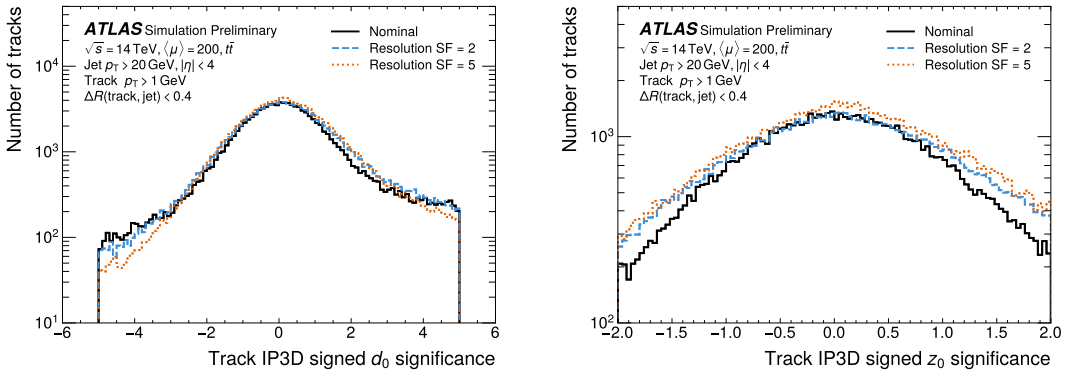

(a) (b)

Figure 25: Distributions of (a) the signed d_0 significance and (b) z_0 significance for tracks associated to jets in the simulated $t\bar{t}$ events that are used for training the b-tagging algorithm, showing the impact of different track resolution degradation scenarios.

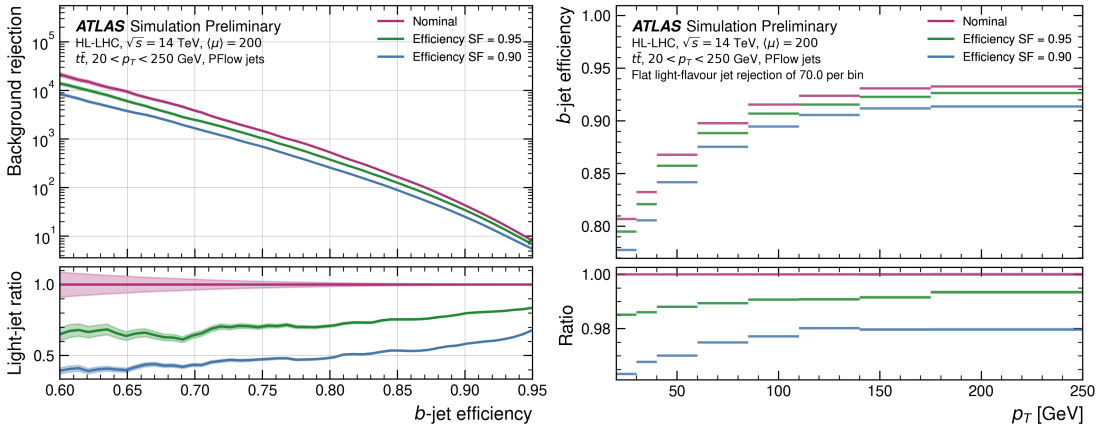

(a) (b)

Figure 26: Performance of the GN2 b-tagging algorithm for different emulated efficiency scale factors (nominal, 95% and 90%): (a) b-jet identification efficiency versus light-flavour jet rejection; (b) b-jet efficiency versus jet p_{T} when light-jet rejection is kept constantly at 70 in each bin.

The performance of the GN2 tagger is studied as a function of different tracking degradation scenarios. Figure 26 shows the impact of different tracking efficiencies (nominal, 95% and 90% efficiency scale factors) on the b-tagging performance. In particular, the left plot shows the ROC for b-tagging efficiency versus light jet rejection, while the right plot shows the b-tagging efficiency that can be achieved as a function of jet p_{T}, when a target rejection of 70 is required in each p_{T} bin.
It can be noted that the observed drop in b-tagging efficiency due to a given reduction of tracking efficiency is largely mitigated by the redundancy of information granted by track multiplicity inside jets. Figure 27 shows equivalent plots for different tracking resolution scenarios (nominal, 1 and 2 resolution scale factors). It can be noted how the degradation of the resolution on impact parameters, being a key ingredient for flavour identification, strongly affects the b-tagging capabilities.
Finally, Figure 28 shows the results for different track p_{T} acceptance configurations. In particular, it compares the offline case, in which no EF Tracking emulation is applied and the cut is consequently set to the default offline reconstruction, with the p_{T} cuts at 1 and 2 GeV expected respectively for full-scan and regional tracking configurations. The latter emulates the fast b-tagging configuration, studied in Ref. [27] for Run 3 trigger operation.
It can be noted how the impact of the full-scan tracking approach is almost negligible with respect to offline operation. The effect is instead more pronounced for the regional tracking option, with most performance degradation impacting the low jet p_{T} region.

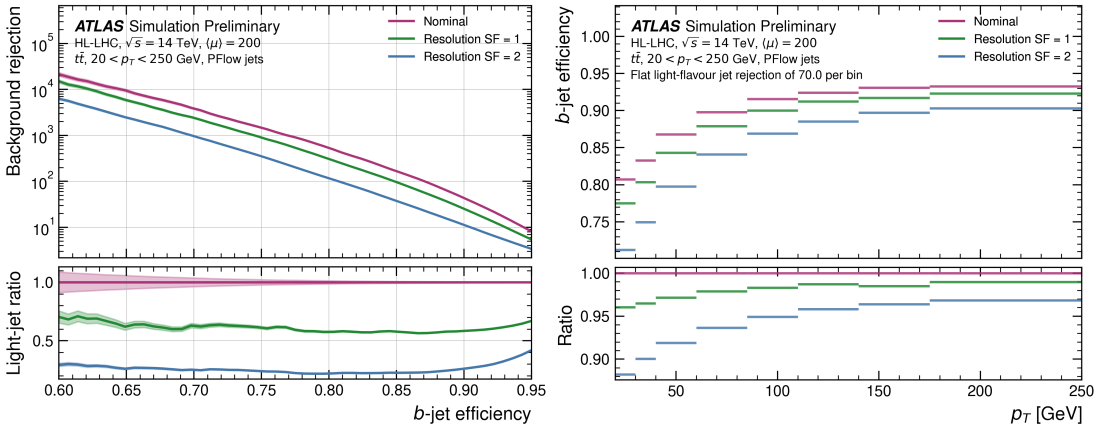

(a) (b)

Figure 27: Performance of the GN2 b-tagging algorithm for different emulated resolution scale factors (nominal, 1 and 2): (a) b-jet identification efficiency versus light-flavour jet rejection; (b) b-jet efficiency versus jet p_{T} when light-jet rejection is kept constantly at 70 in each bin.

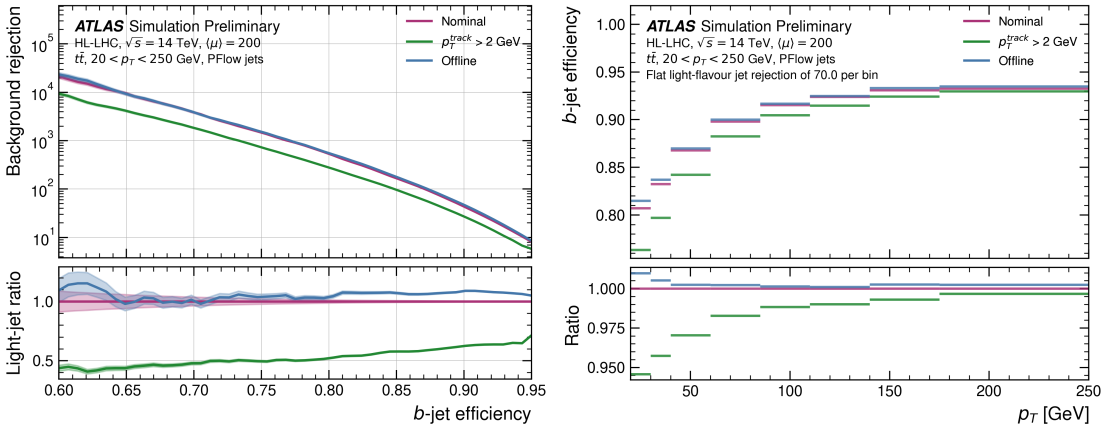

(a) (b)

Figure 28: Performance of the GN2 b-tagging algorithm for different track p_{T} cuts; offline corresponds to the default offline tracking configuration, nominal applies the p_{T} cut at 1 GeV corresponding to the global tracking option, while the cut at 2 GeV is meant to emulate the regional tracking option: (a) b-jet identification efficiency versus light-flavour jet rejection; (b) b-jet efficiency versus jet p_{T} when light-jet rejection is kept constantly at 70 in each bin.

5.6 Missing energy trigger selections

Missing energy triggers foreseen for Run 4 target thresholds around 200 GeV, as mentioned in the representative trigger menu summarized in Table 1. Their performance is expected to be primarily driven by jet reconstruction quality in the calorimeters, but depends also on tracking inputs. As an example, particle-flow jet reconstruction will be adopted for these selections in Run 4. As mentioned for other triggers, the study described in this note does not take into account particle-flow algorithms.

The possible impact of tracking performance on $E_{\mathrm{T}}^{\mathrm{miss}}$ selections is thus assessed comparing different algorithms, some of which use tracks among their inputs. All the algorithms taken under consideration in

this study are variants of the two main algorithms implemented for Run 3 [5, 31]: `Pufit`, which corrects for pile-up effects on high-E_T calorimeter signals, and `MHT`, which uses a negative vector sum of jets that passing a jet-vertex tagger (JVT) [24] selection in the $E_{\mathrm{T}}^{\mathrm{miss}}$ calculation. In particular, the following combined algorithms have been considered:

- `TCPufit`: builds $E_{\mathrm{T}}^{\mathrm{miss}}$ using topo-clusters and subtracts the pile-up contribution derived in high-p_{T} clusters;
- `MHTTopo`: calculates $E_{\mathrm{T}}^{\mathrm{miss}}$ using the vectorial sum of selected jets with $p_{\mathrm{T}} > 50$ GeV and JVT selection; jets are built from EM-scale and hadronic-scale topo-clusters.
- `MHTPufit (Pflow/Topo)`: builds $E_{\mathrm{T}}^{\mathrm{miss}}$ using MHT from jets passing a JVT selection. A similar technique to `TCPufit` is used to estimate pile-up contribution on these jets; jets can be reconstructed either from topo-clusters (Topo) or from particle-flow (Pflow).
- `TrkMHT`: builds $E_{\mathrm{T}}^{\mathrm{miss}}$ from jets identified as coming from the primary vertex, using the JVT selection. Tracks from the primary vertex that are not associated with any jets passed JVT selection are included in the $E_{\mathrm{T}}^{\mathrm{miss}}$ calculation as a track soft term.

Studying the performance of all these algorithms allows a comparison between the first two, purely based on calorimeter-based calculations, with the two latter ones, including tracks among their inputs.

The Level-0 $E_{\mathrm{T}}^{\mathrm{miss}}$ trigger is emulated using offline jets reconstructed by use of topological-clusters with accurate local calibration (either electromagnetic or hadronic, depending on the nature of the cluster). Starting from this, the emulation adopts the `MHTTopo` offline-like algorithm, which reconstructs $E_{\mathrm{T}}^{\mathrm{miss}}$ based on calibrated jets. The Level-0 selection thresholds have been set at 50 GeV for single jets and at 150 GeV for `MHTTopo`, ensuring a 95% Level-0 signal efficiency at 210 GeV, coupled to a rate of 60 kHz, as in the representative trigger menu. The impact of the EF Tracking performance on these online $E_{\mathrm{T}}^{\mathrm{miss}}$ algorithms has been measured:

- on ZH signal events leading to a $\nu\nu bb$ final state;
- on background di-jet events, containing no real $E_{\mathrm{T}}^{\mathrm{miss}}$ contributions.

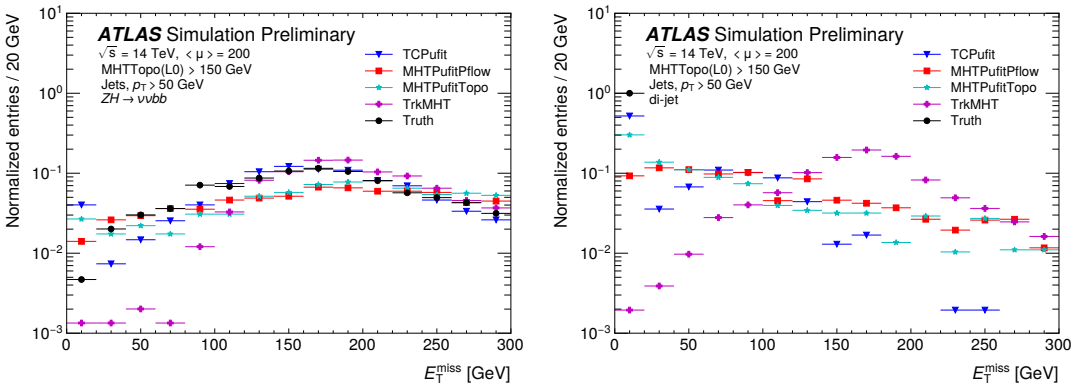

(a) (b)

Figure 29: $E_{\mathrm{T}}^{\mathrm{miss}}$ distributions from four algorithms (`TCPufit`, `MHTPufit`, both `Pflow` and `Topo`, and `TrkMHT`) compared to truth missing energy, for events passing the emulated Level-0 trigger selection (requiring 50 GeV jets and `MHTTopo` > 150 GeV): (a) for signal $ZH \rightarrow \nu\bar{\nu}b\bar{b}$ and (b) for background di-jet samples, both with $\langle\mu\rangle = 200$.

The reconstructed $E_{\mathrm{T}}^{\mathrm{miss}}$ distributions for all these algorithms, compared with truth missing-energy, are shown in Figure 29 on both signal and background samples at $\langle\mu\rangle = 200$. The curves corresponding to $E_{\mathrm{T}}^{\mathrm{miss}}$ calculations for efficiency versus rejection are shown in Figure 30(a), comparing the performance of the four types of $E_{\mathrm{T}}^{\mathrm{miss}}$ algorithms. From the plot it's clear that the `TCPufit` algorithm, based on pure calorimeter information, has largely better background rejection. It's worth noticing that the performance of the `MHTPufit` algorithms could be improved if reconstructed `Pflow` objects are used for pile-up suppression. In this study, instead of `Pflow`, not available in the simulation, reconstructed tracks are used as input to the algorithms.

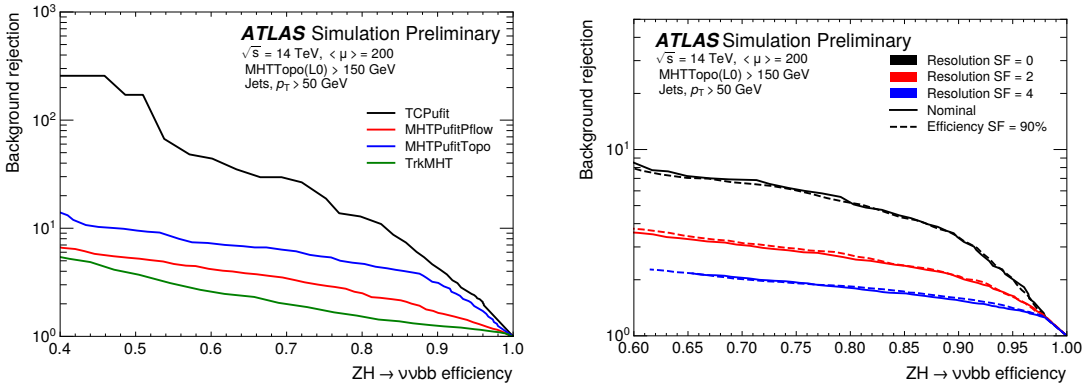

(a) (b)

Figure 30: Efficiency on signal $ZH \rightarrow \nu\bar{\nu}b\bar{b}$ versus di-jet background rejection, at $\langle\mu\rangle = 200$, with emulated Level-0 trigger selection applied on both and taken as reference for the measurements: (a) for four $E_{\mathrm{T}}^{\mathrm{miss}}$ algorithms: `TCPufit`, `MHTPufit` (both `Pflow` and `Topo`), and `TrkMHT`; (b) for the `MHTPufit` algorithm in different emulated tracking scenarios, smearing both the efficiency and the track resolutions.

To study the effect of different EF Tracking performance scenarios, their impact on the particle-flow version of the `MHTPufit` algorithm is considered, focusing on its pile-up suppression, which makes extensive use of the tracks and the jets in the event, to correct for pile-up contributions in jets passed the JVT selection. Figure 30(b) reports the effect of different EF Tracking performance scenarios on the chosen algorithm. While reducing the track reconstruction efficiency has a negligible impact, the resolution smearing introduces an evident degradation of `MHTPufit` performance. This can be explained as a degradation of the track p_{T} estimates that can largely affect the evaluation of the pile-up contribution to selected jets in $E_{\mathrm{T}}^{\mathrm{miss}}$ calculation.

5.7 Long-lived particle trigger selections

The HL-LHC trigger menu does not explicitly contain any selection targeting long-lived particles (LLP). Given their important role in new physics searches, such triggers will be anyway included in the future, exploiting the global rate margins. One of the distinctive signatures of LLP signals is the presence of tracks with very large impact parameters, resulting from their late decays. A specific track reconstruction task focusing on such use case, called Large Radius Tracking (LRT), has been demonstrated in Ref. [2]. These studies also assessed preliminary indications on the event rate for full-scan LRT.

In this note, the impact of the performance for the EF Tracking LRT implementation is studied on a simulated SUSY signal containing a pair of gluinos that decay into a neutralino and two quarks. The neutralinos are afterwards decaying through an R-parity violating coupling into three quarks, with a lifetime of 0.1 ns ($\tilde{g}\tilde{g} \rightarrow qq\tilde{\chi}_1^0 \rightarrow qqqqq$ with $m_{\tilde{g}}$ = 1.6 TeV and $m_{\tilde{\chi}_1^0}$ = 50 GeV). The LLP decay products contain a very large fraction of non-pointing tracks that can be produced beyond the last pixel layer due to the large neutralino boost. The trigger designed for this signal is based on the identification of jets containing displaced tracks; similar triggers are already included in the current Run 3 trigger [5]. Since offline LRT is still under development for the HL-LHC scenario, an alternative emulation strategy is adopted. Truth particles are used as a proxy for offline-reconstructed LRT tracks and are consequently smeared to emulate a degraded EF Tracking LRT reconstruction. This allows to compare emulated offline and online tracking, with and without LRT capability. This study also assumes that the tracking efficiency is reduced for large gluino production radii, as a consequence of the increasing computing resources needed to reconstruct tracks with large displacements, compared to the standard tracking.

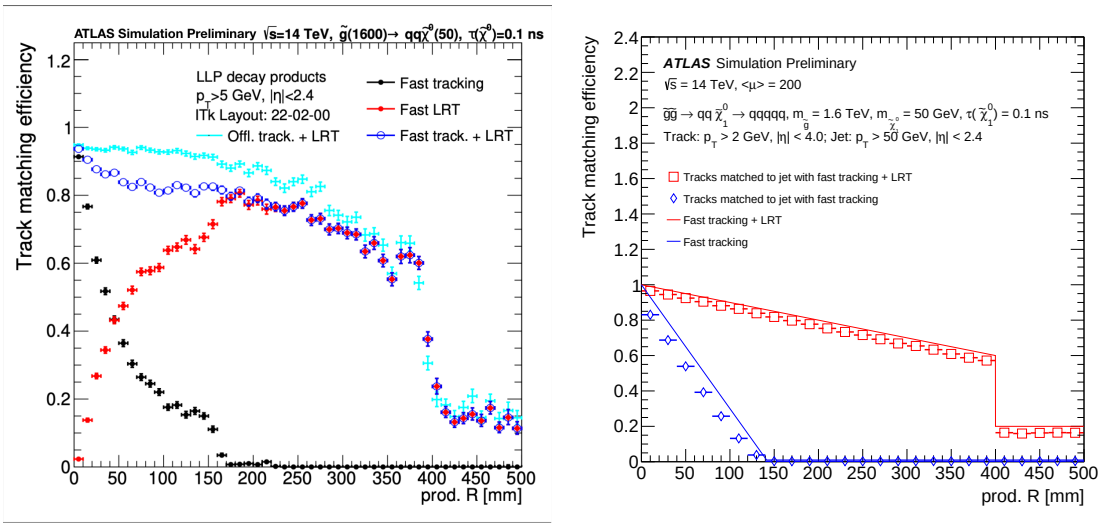

(a) (b)

Figure 31: (a) Track-matching efficiency of tracking algorithms extracted from Ref. [2], comparing the standard offline tracking and a fast tracking version of it, with and without the LRT extensions, on the chosen signal sample. (b) Track-matching efficiency reproduced in this study including two parameterisations of the single track efficiency of the fast trigger tracking with and without the LRT extensions. The extracted efficiency in the same signal sample obtained with emulated EF Tracking tracks reproducing the two scenarios by the use of these functions are also superimposed.

Results from Ref. [2] are taken as reference and in particular Figure 31(a) reported here, which shows the track-matching efficiency as a function of the true particle production radius (referred as prod. R) for the offline tracking with LRT capability and the corresponding online fast-tracking option (which is the software tracking version studied for the trigger in [2]), with and without the LRT inclusion. To reproduce this scenario, that is the result of a possible detailed simulation of a fast-tracking algorithm on a specific SUSY sample, the same sample is chosen and the same efficiency behavior is emulated, with a simple approach. The fast-tracking efficiency curves with and without the LRT component in that plot are approximated with analytic functions that reproduce the same shape, and the chosen parameterisations are shown in Figure 31(b). These parameterisations are included in the EF Tracking emulation tool as variable tracking efficiency scale factors on truth particle, with exactly the same mechanism as the other studies, but

changing with the particle production radius.

Starting from these ingredients, a possible LLP trigger is emulated. The Level-0 is emulated following the approach already used in Run 3 for similar selections, and simply retaining events with at least one jet with $p_{\mathrm{T}} > 160\,\mathrm{GeV}$. At the EF, emulated tracks with $p_{\mathrm{T}} > 1\,\mathrm{GeV}$ and $|\eta| < 4.0$ are matched to jets within a cone of $\Delta R < 0.4$. Figure 31(b) shows the resulting track-to-jet matching efficiencies, excluding and including the LRT component. Jets are then classified based on the number of prompt and displaced tracks they contain. Tracks with $|d_0| < 3\,\mathrm{mm}$ and $|z_0 \sin(\theta)| < 3$ are considered prompt, while tracks with $|d_0| \geq 3\,\mathrm{mm}$ are considered displaced. A jet is considered displaced if it has $p_{\mathrm{T}} > 50\,\mathrm{GeV}$ and contains at least two displaced tracks and at most two prompt tracks (so called "2d2p" requirement). Such requirement is motivated by the distributions of the number of prompt and displaced tracks associated to signal jets, that are shown in Figure 32(a). In this figure, the number of matched tracks, both prompt and displaced, emulated by the fast-tracking with LRT extension, is similar to that of the charged particles.

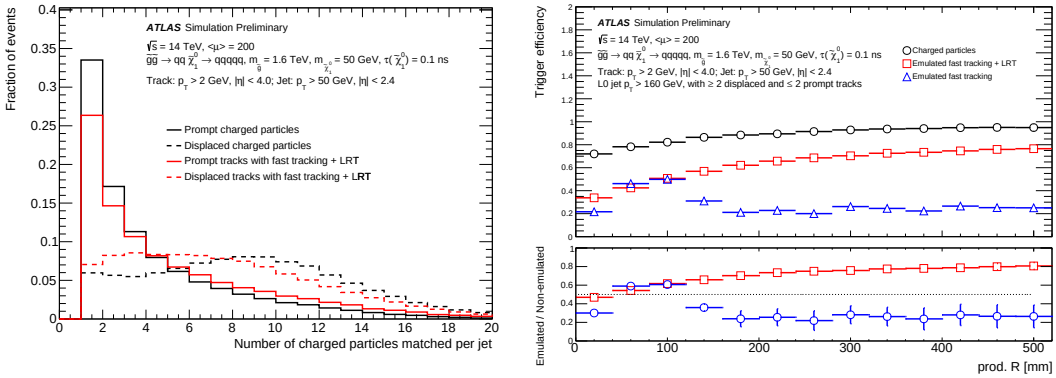

(a) (b)

Figure 32: (a) Number of charged particles with $p_{\mathrm{T}} > 2$ GeV, associated to a LLP jet from the gluino decay, for jets above 50 GeV. Different classes of particles are shown: prompt have $|d_0| < 3\,\mathrm{mm}$ and $|z_0 \sin(\theta)| < 3$, those with $|d_0| \geq 3\,\mathrm{mm}$ are defined as displaced, with and without the emulated parameterization. (b) Displaced-jet trigger efficiency as a function of the gluino production radius, with and without the track emulation. Efficiency is measured on the signal sample at $\langle\mu\rangle = 200$, with respect to the emulated Level-0 (which selects events with at least one jet with $p_{\mathrm{T}} > 160\,\mathrm{GeV}$), by requiring that at least one jet has minimum two displaced tracks and maximum two prompts tracks ("2d2p"). The bottom panel displays the ratios of trigger efficiencies for various track emulation settings compared to the trigger efficiency without any track emulation.

Plots of the resulting trigger efficiency are shown in Figure 32(b), comparing the selection based on emulated EF Tracking tracks with and without LRT to that based on truth particle, corresponding to an ideal tracking performance. These results demonstrate how the efficiency at large production radius is enhanced when the LRT tracking capabilities are included. Figure 32(b) also demonstrates that the efficiency ratio between the ideal case and the realistic one including LRT is almost constant over the investigated production radius range, regardless of the LRT efficiency drop for a radius around 400 mm shown in Figures 31(a) and 31(b). This is because the multiplicity of tracks matched to jets, shown in Figure 32(a), is enough to satisfy the trigger conditions, including not only tracks coming from the neutralino, but also from the rest of the event.

6 Conclusions

The studies described in this note relate various plausible EF Tracking performance to their impact on the main trigger signatures defined in the representative trigger menu in Table 1. The trigger selections are chosen as to cover different tracking regimes. For example, single leptons, like muons and electrons, have stronger requirements on high momentum tracks, while hadronic selections, like $E_{\mathrm{T}}^{\mathrm{miss}}$, multi-jets, b-tagging and hadronic τ selections, are more impacted by tracking performance at low p_{T} and in particular by the track impact parameter resolution. Some investigations on the long-lived particle (LLP) selections, which are becoming more and more important for the HL-LHC discovery plans, are also included with a simplified approach.

The performance of these trigger selections are assessed adopting a tracking emulation strategy that recreates degraded EF Tracking scenarios, in most cases starting from offline tracks, covering both regional and full-scan tracking options. It emulates a worsening of the tracking algorithms at large η and at low momentum, following the offline-tracking behavior. In particular, the effects of a reduced tracking reconstruction efficiency and of a worsened resolution on track parameters are investigated. For some trigger selections, a track duplication approach is also adopted to investigate the impact on the isolation selection, which depends on the track multiplicity in a ΔR cone around the reference particle.

With all the necessary caveats related to the emulation of the Level-0 selection that selects the regions for the tracking processing, all the algorithms investigated in this note, adopted in Run 3 for the reconstruction of physics objects and adapted to work with the ITk geometry in the HL-LHC environment, show a high level of robustness against possibly imperfect EF Tracking track quality. For most of them, when the background representation is considered reliable, the background rejection is evaluated as well, as counterpart of the signal efficiency. As a summary of these studies, no dramatic degradation is observed for any trigger signature under consideration, when the following EF Tracking working points are ensured:

- EF Tracking is working both in full-scan and in regional tracking, with implicit minimum track p_{T} requirement of 1 GeV and 2 GeV, respectively;
- EF Tracking efficiency is at least 98% and 95% with respect to offline tracking for high-p_{T} (> 10 GeV) and low-p_{T} (< 10 GeV) regime, respectively;
- EF Tracking resolution on track parameters (p_{T}, d_0, z_0) is up to a factor two worse than offline tracking;
- EF Tracking provides up to a 1% increase in the duplicate tracks rate with respect to offline tracks.

References

[1] ATLAS Collaboration, *The ATLAS Experiment at the CERN Large Hadron Collider*, JINST **3** (2008) S08003 (cit. on p. 2).

[2] ATLAS Collaboration, *Technical Design Report for the Phase-II Upgrade of the ATLAS Trigger and Data Acquisition System - Event Filter Tracking Amendment*, (2022), URL: https://cds.cern.ch/record/2802799 (cit. on pp. 2–4, 35, 40, 41).

[3] ATLAS Collaboration, *ATLAS Inner Tracker Strip Detector: Technical Design Report*, ATLAS-TDR-025; CERN-LHCC-2017-005, 2017, URL: https://cds.cern.ch/record/2257755 (cit. on pp. 2, 3).

[4] ATLAS Collaboration, *ATLAS Inner Tracker Pixel Detector: Technical Design Report*, ATLAS-TDR-030; CERN-LHCC-2017-021, 2017, URL: https://cds.cern.ch/record/2285585 (cit. on pp. 2, 3).

[5] ATLAS Collaboration, *The Run-3 ATLAS Trigger System*, (2022), URL: https://cds.cern.ch/record/2845056 (cit. on pp. 2, 35, 39, 41).

[6] ATLAS Collaboration, *ATLAS TDAQ Phase-II Upgrade: Technical Design Report*, ATLAS-TDR-029; CERN-LHCC-2017-020, 2017, URL: https://cds.cern.ch/record/2285584 (cit. on pp. 2, 19).

[7] S. Frixione, G. Ridolfi and P. Nason, *A positive-weight next-to-leading-order Monte Carlo for heavy flavour hadroproduction*, JHEP **09** (2007) 126, arXiv: 0707.3088 [hep-ph] (cit. on p. 5).

[8] T. Sjöstrand, S. Mrenna and P. Skands, *PYTHIA 6.4 physics and manual*, JHEP **05** (2006) 026, arXiv: hep-ph/0603175 (cit. on p. 5).

[9] S. Agostinelli et al., *GEANT4 – a simulation toolkit*, Nucl. Instrum. Meth. A **506** (2003) 250 (cit. on p. 5).

[10] ATLAS Collaboration, *The ATLAS Simulation Infrastructure*, Eur. Phys. J. C **70** (2010) 823, arXiv: 1005.4568 [physics.ins-det] (cit. on p. 5).

[11] ATLAS Collaboration, *Expected Tracking Performance of the ATLAS Inner Tracker at the HL-LHC*, ATL-PHYS-PUB-2019-014, 2019, URL: https://cds.cern.ch/record/2669540 (cit. on p. 5).

[12] ATLAS Collaboration, *Expected tracking and related performance with the updated ATLAS Inner Tracker layout at the High-Luminosity LHC*, ATL-PHYS-PUB-2021-024, 2021, URL: https://cds.cern.ch/record/2776651 (cit. on p. 5).

[13] ATLAS Collaboration, *Software and computing for Run 3 of the ATLAS experiment at the LHC*, (2024), arXiv: 2404.06335 [hep-ex] (cit. on p. 5).

[14] ATLAS Collaboration, *Performance studies of tracking-based triggering using a fast emulation*, ATL-DAQ-PUB-2023-001, 2023, URL: https://cds.cern.ch/record/2848431 (cit. on pp. 6, 29).

[15] ATLAS Collaboration, *Expected performance of the ATLAS detector under different High-Luminosity LHC conditions*, ATL-PHYS-PUB-2021-023, 2021, URL: https://cds.cern.ch/record/2765851 (cit. on p. 12).

[16] ATLAS Collaboration, *Improved electron reconstruction in ATLAS using the Gaussian Sum Filter-based model for bremsstrahlung*, ATLAS-CONF-2012-047, 2012, URL: https://cds.cern.ch/record/1449796 (cit. on p. 13).

[17] ATLAS Collaboration, *Electron and photon performance measurements with the ATLAS detector using the 2015–2017 LHC proton–proton collision data*, JINST **14** (2019) P12006, arXiv: 1908.00005 [hep-ex] (cit. on p. 14).

[18] ATLAS Collaboration, *Reconstruction, Identification, and Calibration of hadronically decaying tau leptons with the ATLAS detector for the LHC Run 3 and reprocessed Run 2 data*, ATL-PHYS-PUB-2022-044, 2022, URL: https://cds.cern.ch/record/2827111 (cit. on pp. 18, 19).

[19] ATLAS Collaboration,
Topological cell clustering in the ATLAS calorimeters and its performance in LHC Run 1,
Eur. Phys. J. C **77** (2017) 490, arXiv: 1603.02934 [hep-ex] (cit. on pp. 18, 28).

[20] ATLAS Collaboration, *Determination of jet calibration and energy resolution in proton–proton collisions at* $\sqrt{s} = 8$ *TeV using the ATLAS detector*, Eur. Phys. J. C **80** (2020) 1104,
arXiv: 1910.04482 [hep-ex] (cit. on p. 18).

[21] M. Cacciari, G. P. Salam and G. Soyez, *SoftKiller, a particle-level pileup removal method*,
Eur. Phys. J. C **75** (2015) 59, arXiv: 1407.0408 [hep-ph] (cit. on pp. 28, 29).

[22] ATLAS Collaboration, *Jet energy scale and resolution measured in proton–proton collisions at* $\sqrt{s} = 13$ *TeV with the ATLAS detector*, Eur. Phys. J. C **81** (2021) 689,
arXiv: 2007.02645 [hep-ex] (cit. on p. 29).

[23] P. T. Komiske, E. M. Metodiev and J. Thaler, *Energy Flow Networks: Deep Sets for Particle Jets*,
JHEP **01** (2019) 121, arXiv: 1810.05165 [hep-ph] (cit. on p. 29).

[24] ATLAS Collaboration, *Tagging and suppression of pileup jets with the ATLAS detector*,
ATLAS-CONF-2014-018, 2014, URL: https://cds.cern.ch/record/1700870
(cit. on pp. 29, 32, 39).

[25] ATLAS Collaboration,
Deep Sets based Neural Networks for Impact Parameter Flavour Tagging in ATLAS,
ATL-PHYS-PUB-2020-014, 2020, URL: https://cds.cern.ch/record/2718948
(cit. on p. 32).

[26] ATLAS Collaboration, *Configuration and performance of the ATLAS b-jet triggers in Run 2*,
Eur. Phys. J. C **81** (2021) 1087, arXiv: 2106.03584 [hep-ex] (cit. on p. 35).

[27] ATLAS Collaboration,
Fast b-tagging at the high-level trigger of the ATLAS experiment in LHC Run 3,
JINST **18** (2023) P11006, arXiv: 2306.09738 [hep-ex] (cit. on pp. 35, 37).

[28] ATLAS Collaboration, *Graph Neural Network Jet Flavour Tagging with the ATLAS Detector*,
ATL-PHYS-PUB-2022-027, 2022, URL: https://cds.cern.ch/record/2811135
(cit. on p. 35).

[29] ATLAS Collaboration, *Neural Network Jet Flavour Tagging with the Upgraded ATLAS Inner Tracker Detector at the High-Luminosity LHC*, ATL-PHYS-PUB-2022-047, 2022,
URL: https://cds.cern.ch/record/2839913 (cit. on p. 35).

[30] ATLAS Collaboration, *Jet Flavour Tagging With GN1 and DL1d. Generator dependence, Run 2 and Run 3 data agreement studies*,
https://atlas.web.cern.ch/Atlas/GROUPS/PHYSICS/PLOTS/FTAG-2023-01/
(cit. on p. 35).

[31] ATLAS Collaboration, *Performance of the missing transverse momentum triggers for the ATLAS detector during Run-2 data taking*, JHEP **08** (2020) 080, arXiv: 2005.09554 [hep-ex]
(cit. on p. 39).